



3D Cementitious composites printing with pretreated recycled crumb rubber: mechanical and acoustic insulation properties

Xiangyu Wang, Liangfen Du, Zhenbang Liu, Mingyang Li, Yiwei Weng, Zhixin Liu, Yi Wei Daniel Tay, Zheng Fan, Teck Neng Wong & Ming Jen Tan

To cite this article: Xiangyu Wang, Liangfen Du, Zhenbang Liu, Mingyang Li, Yiwei Weng, Zhixin Liu, Yi Wei Daniel Tay, Zheng Fan, Teck Neng Wong & Ming Jen Tan (2024) 3D Cementitious composites printing with pretreated recycled crumb rubber: mechanical and acoustic insulation properties, *Virtual and Physical Prototyping*, 19:1, e2399787, DOI: [10.1080/17452759.2024.2399787](https://doi.org/10.1080/17452759.2024.2399787)

To link to this article: <https://doi.org/10.1080/17452759.2024.2399787>



© 2024 The Author(s). Published by Informa UK Limited, trading as Taylor & Francis Group



[View supplementary material](#)



Published online: 09 Sep 2024.



[Submit your article to this journal](#)



Article views: 589



[View related articles](#)



[View Crossmark data](#)

3D Cementitious composites printing with pretreated recycled crumb rubber: mechanical and acoustic insulation properties

Xiangyu Wang^a, Liangfen Du^c, Zhenbang Liu^a, Mingyang Li^{ib a}, Yiwei Weng^d, Zhixin Liu^e, Yi Wei Daniel Tay^{ib a}, Zheng Fan^b, Teck Neng Wong^a and Ming Jen Tan^a

^aSingapore Centre for 3D Printing, School of Mechanical and Aerospace Engineering, Nanyang Technological University, Singapore, Singapore; ^bSchool of Mechanical and Aerospace Engineering, Nanyang Technological University, Singapore, Singapore; ^cDepartment of Building Environment and Energy Engineering, The Hong Kong Polytechnic University, Hong Kong, People's Republic of China; ^dDepartment of Building and Real Estate, The Hong Kong Polytechnic University, Hong Kong, People's Republic of China; ^eChina Aerospace Times Feihong Technology Corporation Limited, Beijing, People's Republic of China

ABSTRACT

Cementitious materials incorporating recycled crumb rubber have become a common sustainable resolution in diverse building environments to achieve various functions in terms of lightweight, ductility, as well as energy absorption. This study explored the 3D printed rubberised cementitious composites (3DPRC) in two aspects: examining the effects of crumb rubber pretreatment conditions on compressive properties; conducting experimental and numerical analysis on the acoustic dissipation characteristics of 3DPRC. Fine crumb rubber granules (3-5 mm) replaced 10%, 20%, and 30% of river sand in the composites. Uniaxial compression tests indicated that the compressive strength of 3DPRC decreased with the increase of crumb rubber content and introduced anisotropic behaviour. Impedance tube tests were conducted to evaluate the sound absorption and insulation capabilities of 3DPRC. An optimal Noise Reduction Coefficient (NRC) of 0.35 was achieved with 30% crumb rubber. The sound insulation properties depend strongly on the mass density and porosity of the 3DPRC. Additionally, it is proved that the volume of built-in air gap has positive effects on both sound absorption and insulation properties. The results from Finite Element Method (FEM) numerical simulations correlated well with experimental data, proving the efficiency of the simulation and validating the experimental results.

ARTICLE HISTORY

Received 27 May 2024
Accepted 22 August 2024

KEYWORDS

Crumb rubber; 3D cementitious material printing; compressive strength; sound absorption and isolation



Nomenclature


| | |
|--------------------------|---|
| 3DPRC | 3D Printed Rubberised Cementitious Composites |
| NRC | Noise Reduction Coefficient |
| SAC | Sound Absorption Coefficient |
| CR | Crumb Rubber |
| CT | Computed Tomography |
| STL | Sound Transmission Loss |
| t | Transmission coefficient |
| R | Sound reflection coefficient |
| α | Sound absorption coefficient |
| D_{10}, D_{50}, D_{90} | Characterised particle sizes |
| UCTs | Uniaxial Compressive Tests |
| LVDTs | Linear Variable Differential Transformers |
| ρ | Equivalent Density |
| K | Bulk Modulus |
| s' | Anisotropy Factor |
| ε_p | Porosity |

| | |
|-----------------|-------------------------------|
| τ_{∞} | Tortuosity |
| R_f | Flow Resistivity |
| P_{scat} | Scattered Pressure |
| P_{inc} | Incident Pressure |
| SPL | Sound Pressure Level |
| V_0 | Volume of Cavity |
| L_0 | Length of Channel |
| S_0 | Width of Channel |
| f | Resonance Frequency |
| σ | Relative Compressive strength |
| M_{CR} | Crumb Replacement Fraction |

1. Introduction

The accelerated growth of the global economy and advancements in science and technology have led to widespread urbanisation in economically prosperous regions worldwide. However, this rapid urbanisation has brought the challenge of noise pollution, stemming

CONTACT Mingyang Li  limingyang@ntu.edu.sg  Singapore Centre for 3D Printing, School of Mechanical and Aerospace Engineering, Nanyang Technological University, 50 Nanyang Avenue, Singapore, Singapore

 Supplemental data for this article can be accessed online at <https://doi.org/10.1080/17452759.2024.2399787>.

© 2024 The Author(s). Published by Informa UK Limited, trading as Taylor & Francis Group

This is an Open Access article distributed under the terms of the Creative Commons Attribution License (<http://creativecommons.org/licenses/by/4.0/>), which permits unrestricted use, distribution, and reproduction in any medium, provided the original work is properly cited. The terms on which this article has been published allow the posting of the Accepted Manuscript in a repository by the author(s) or with their consent.

from construction, industrial operations, and transportation, which has considerable implications for both human health and the environment. A study conducted by the National University of Singapore indicated that the average outdoor sound level throughout the day exceeds 69.4 decibels, approaching the World Health Organisation's (WHO) threshold of 70.0 dB per day [1]. Furthermore, continuous low-frequency noise (<1000 Hz) emanated by road traffic, the main source of urban noise, is found to be more likely to increase the risk of cardiovascular morbidity and mortality, as evidenced by prior research [2, 3]. This impact can be ascribed to the difficulties in attenuating low-frequency noise. Such noise exhibits increased transmission capabilities compared to noise with middle and high frequencies through barriers and demonstrates reduced attenuation [4].

In recent years, numerous studies have explored the development of recycled aggregates and their integration into concrete, including the research focusing on their macroscopic mechanical and functional properties [5–7], and research on the microscopic characteristics of fiber-reinforced recycled aggregate concrete [8]. To address above mentioned challenge, the utilisation of cementitious materials with natural aggregates replaced by ground end-of-life tire particles emerges as a possible approach, which not only facilitates the recycling of waste rubber tires but also enhances sound insulation properties due to the high vibroacoustic damping characteristics of such materials. As exemplified by the study conducted by Wang et al. [9], which examined the acoustic performance across a frequency range spanning from 0 Hz to 4000 Hz, cast concrete specimens incorporating rubber particles at replacement rates ranging from 10% to 30% exhibited a 33% to 460% increase of sound absorption capabilities compared to plain concrete. However, conventional cast concrete exhibits limited acoustic absorption capabilities, with a Noise Reduction Coefficient (NRC) typically ranging from 0.03–0.19 [9–11], when compared to traditional acoustic absorptive materials like sponges, acoustic foam panels, and perforated metal panels. Additionally, increasing the crumb rubber content is known to adversely affect the mechanical properties of concrete, as noted by Assgaf et al. [12]. This compromise in mechanical strength for enhanced acoustic absorption in rubberised concrete results in reduced eco-sustainability efficiency. Moreover, achieving improved sound insulation through complex geometric designs in conventional cast concrete can produce additional costs. These factors may limit the broader industrial application of sound insulation rubberised cast concrete. Furthermore, there have been limited reports on the relationship between microstructure and the sound

absorption and insulation properties of 3D printed rubberised concrete. Therefore, to further enhance the sound absorption capability of concrete panels, 3D cementitious composites printing, as an innovative manufacturing technique, is found to possess higher porosity and distinct pore morphology, which is critical in enhancing sound absorption performance.

Recently, the field of 3D cementitious composites printing has advanced quickly, overcoming the limitations associated with traditional concrete methods. These advancements offer several benefits, such as increased energy efficiency [13], cost savings, design flexibility [14], and automated manufacturing [15], as evidenced by research studies [16–19]. Furthermore, a noteworthy aspect is a synergy between printable cementitious materials mixed with recycled lightweight aggregates (crumb rubber) and the numerically controlled additive manufacturing technology. This synergy enables the development of functional cementitious structures with free-form designs characterised by improved energy insulation attributes [20]. Apart from the free-form design, it should be mentioned that the unique characteristics of microscopic pores, a key factor enhancing sound absorption performance in cementitious materials, differ in 3D printed concrete compared to cast concrete [21]. This discrepancy arises from the layer-by-layer extrusion process employed in 3D printing, which lacks compaction [22]. Furthermore, the relationship between the anisotropy properties of 3DPC and the orientation, and morphology of the microscopic pores has been quantitatively investigated based on experiments and simulation [23]. Investigation of the relationship between the pore distribution along the Z-direction and weak interlayer strength of 3DPC was also conducted by Liu et al. [24]. However, there is limited research focusing on the relationship between microscale pore characteristics and the sound absorption mechanism of 3DPRC when subjected to normal incident sound waves. Furthermore, there is a notable lack of research on the impact of varying crumb rubber replacement ratios on the sound absorption properties at low frequencies in 3D printed cementitious composites.

To address the identified research gaps, this study adopted pretreated crumb rubber granules to partially substitute river sand to develop a 3D-printed rubberised cementitious material. Compressive strength and stress-strain relationships that considered pretreatment methods and rubber content of 3DPRC were evaluated systematically. Meanwhile, Scanning Electron Microscopy (SEM) was employed to further discuss the mechanisms of mechanical properties of 3DPRC from a microstructural viewpoint. Impedance tube tests were utilised to

examine the sound absorption and insulation characteristics of 3DPRC, which were analyzed in relation to the CR content and thickness of the built-in air cavity. To further explain the mechanisms of the acoustic absorption of 3DPRC based on overall porosity and pore morphology, X-ray μ CT was conducted. Apart from this, numerical simulations, utilising parameters of the material properties and pore characteristics, were conducted to validate and explain the sound absorption behaviours of 3DPRC.

2. Research significance

To address the limited sound absorption performance of conventional cast concrete and to explore the relationship between microstructure and acoustic properties of 3D printed rubberised concrete, this study will both experimentally and numerically examine the effects of crumb rubber content and built-in air gaps on the acoustic absorption and insulation performance of 3D printed rubberised cementitious composites (3DPRC). Additionally, the impact of pretreatment methods and crumb rubber content on the mechanical properties of 3DPRC will be assessed. The study aims to identify the optimal crumb rubber replacement ratio, integrating findings from acoustic and mechanical testing. The results are intended to provide technical support for the application of free-form designed 3D printed sound absorption concrete walls and other relevant engineering applications.

3. Acoustic theory

In this study, the investigation focuses on the noise-attenuating properties of 3DPRC blocks containing elongated pores. This section describes the experimental measurement of sound transmission loss (STL) and sound absorption coefficient (SAC) using the transfer function method under normal incidence conditions.

The approach for measuring acoustic transmission loss, as specified in the ASTM E2611 standard [25], assumes that the sound field in both the upstream and downstream sections of the standing wave tube can be accurately approximated by combinations of positive – and negative-directed plane waves. As illustrated in Figure 1a, two microphones were positioned in the upstream section, and two additional ones are situated in the downstream area. To ensure variation in loads across the entire frequency spectrum, a reactive load, symbolising a rigid termination, and an absorbing load, symbolising a rigid end equipped with sponge foam, were employed.

With the aid of transfer function method, the normal incidence transmission loss (TL_n) of the tested specimen

can be calculated as follows:

$$TL_n = 20 \log_{10} |t| \quad (1)$$

Where t represents transmission coefficient calculated by transfer function method, where the derivation process can be found in ASTM E2611 standard. The sound-absorbing capability of the 3D printed specimen is characterised by its SAC, which quantifies the proportion of sound energy that is not reflected from the surface to the incident sound intensity. The transfer function method is applied to experimentally determine the SAC, as illustrated in Figure 1b. In accordance with ISO 10534–2 standard [26], one can calculate the sound absorption coefficient (α) using the formula:

$$\alpha = 1 - |R|^2 \quad (2)$$

where R represents the sound reflection coefficient that signifies the proportion of the reflected sound intensity to the total incident sound intensity.

4. Materials and methods

4.1. Mixture design and pretreatment conditions

Table 1 provides information about the mixture design for the 3D printable mortars, which consists of premix cement, which was utilised in the literature conducted by Liu et al. [18, 23], (PHOENIX Portland Composite-LAFARGE, Buildmate PTE. LTD, Singapore), river sand with particle size ≤ 2 mm, waste crumb rubber (CR) granules with the density of 1130 kg/m^3 and water absorption rate of 1.5% (Huabang Mineral Products Co., Ltd. China), silica fume (Microsilica Grade 940, Elkem company, Singapore) and water. Ten cases were investigated in this study, including 'Control (3D printed cementitious composites without CR)', 'UN10 (3DPRC with 10% untreated CR)', 'W10 (3DPRC with 10% water treated CR)', 'NA10 (3DPRC with 10% NaOH treated CR)'. In this research, it is imperative to emphasise that the water-to-binder ratio is held constant across all formulated mixtures, maintaining a fixed value of 0.305. River sand with weight fractions of 10%, 20%, and 30% are replaced by CR granules with a density of 1100 kg/m^3 . The method to evaluate the rheological properties of the well-defined mix design was introduced in section 1.1 of supplementary information and test protocol was illustrated in Figure S1. The particle size distribution of the aggregates, comprising river sand and crumb rubber particles, is depicted in Figure 2. It can be found that the particle size distribution curves are kept within reasonable boundary conditions according to China standard GB/T 14684 [27]. The river sand employed in this study is classified as fine sand with

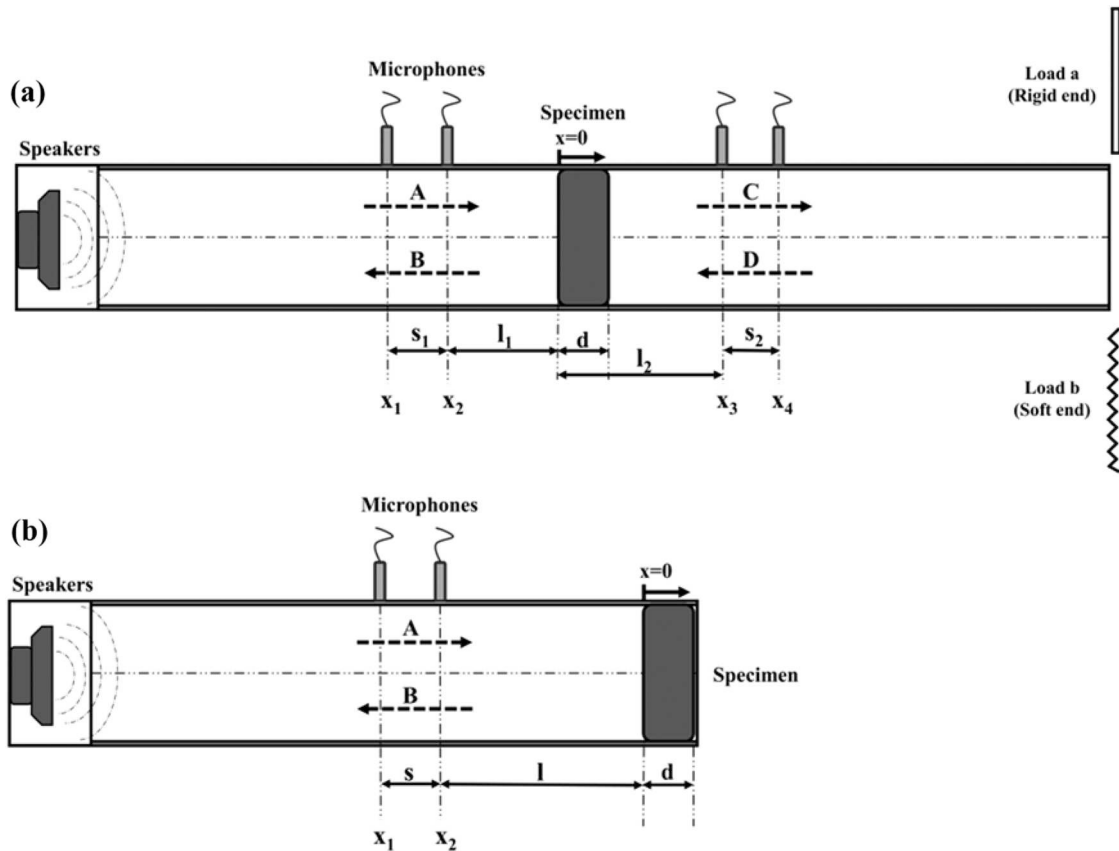


Figure 1. Schematics of transfer function methods (a) the measurement of STL; (b) the measurement of SAC; X_1 to X_4 corresponds to positions of 1st to 4th microphone.

the modulus of fineness of 1.99, and the nominal particle diameter is smaller than 4.75 mm. A similar analysis method was also proposed in the studies conducted by Wang et al. [28]. Given the grading differences between river sand and crumb rubber, it is evident that river sand encompasses a broader range of particle sizes, which effectively fills voids and contributes to a denser, more compact concrete structure. In contrast, crumb rubber is characterised by a more uniform, narrow grading that tends to increase voids within the concrete. Consequently, substituting river sand with crumb rubber in concrete formulations generally results in decreased overall strength and increased deformation, attributed to the higher damping

properties of crumb rubber. From Table 2, it is shown that the characterised particle sizes (D_{10} , D_{50} , and D_{90}) of the aggregates in this mixture, which underpin the numerical analysis on the acoustic absorption performance of the specimens in Section 5. In this investigation, the size range of employed CR falls within 0.60–2.36 mm, which aligns with the specifications used in prior research conducted by Liu et al. [29].

Regarding the surface modification of CR, this study incorporates two distinct pretreatment methodologies: water treatment and NaOH treatment. The workflow for these two pretreatment methods is shown in Figure 3. In the case of water treatment, rubber granules were placed within a sieve and subjected to rinsing with tap water until the absence of any residual black dust in the drained water was observed. Following this washing process, the granules were subjected to air drying before mixing. In contrast, the NaOH treatment involves initially washing the CR granules with tap water in a sieve tray. Subsequently, the granules were immersed in a 10% concentration NaOH solution for 0.5 hours. It is noteworthy that the optimal pretreatment efficacy, as explained in a prior investigation by Youssf et al. [30], is attained when the soaking period is precisely 0.5

Table 1. Mass proportion (kg/m^3) of the printable mortar for the control and crumb rubber groups (Water/Binder = 0.305).

| Mixture | Premix Cement | River Sand (0–2 mm) | Crumb Rubber (0.6–3 mm) | Silica Fume | Water |
|-----------|---------------|---------------------|-------------------------|-------------|-------|
| Control | 1151.3 | 590 | 0 | 28.8 | 360 |
| UN/W/NA10 | 1151.3 | 531 | 59 | 28.8 | 360 |
| UN/W/NA20 | 1151.3 | 472 | 118 | 28.8 | 360 |
| UN/W/NA30 | 1151.3 | 413 | 177 | 28.8 | 360 |

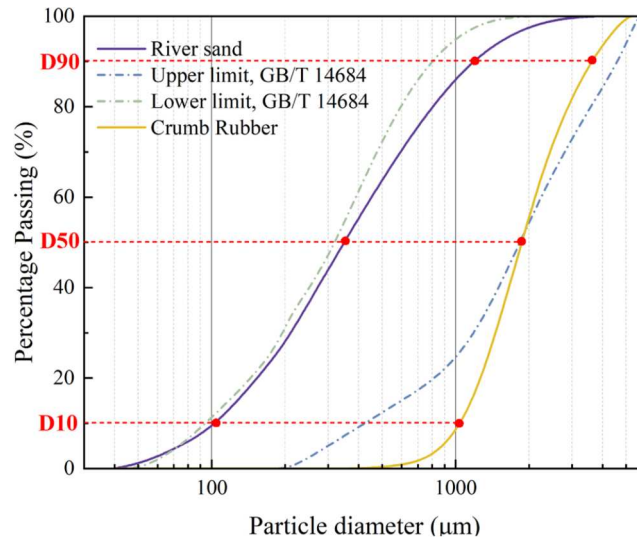


Figure 2. Particle size distribution of aggregates (River sand and Crumb rubber).

hours. Following immersion, the granules are thoroughly washed with tap water for 30 minutes to eliminate any remaining NaOH solution, mitigating potential adverse effects on concrete durability.

While immersed in the NaOH solution, a chemical reaction occurs between NaOH and the hydrophobic aromatic oil and zinc stearate present on the surface of the crumb rubber, which results in the removal of such non-polar substances. Consequently, the surface characteristics of the rubber particles are noticeably altered. Specifically, a cleaner and rougher surface can be observed in comparison to rubber particles subjected to water washing or untreated conditions, which also leads to the formation of additional voids on the rubber surface. It is evident from the comparative analysis between Figure 4a (untreated rubber) and Figure 4b (rubber treated with NaOH) that the latter exhibits a more porous surface.

4.2. 3D cementitious composites printing characteristics

A three-axis gantry printer featuring a circular nozzle, as depicted in Figure 5, was employed for 3D cementitious composites printing. The gantry printer boasts a maximum printing volume of 1.2 m × 1.2 m × 1.0 m (L × W × H). To facilitate material delivery, a 3-meter-

long delivery hose with an inner radius of 12.7 mm connected the printing head to a rotor-stator pump, specifically the MAI-2 Pictor Pump. This setup delivers well-mixed fresh cementitious mortar from the material container through the hose to the nozzle head with a constant volumetric flow rate of 1.2 L/min. The nozzle, which maintained a consistent material output, moved at a travel speed of 100 mm/s following a pre-designed programme. This allowed for the accurate construction of the intended structure.

Figure 6(a) & (b) illustrate the geometric specifications of the 3DPRC block, both in its design for printing and as physically printed samples. 3D printed specimens are rectangular blocks, featuring a cross-sectional dimension of 140 mm × 140 mm (W × H) and incorporating distinct built-in air cavity volumes. To assess the influence of the air cavity within the structure on acoustic absorption properties, three sets of samples with thicknesses of air cavity were set at 0, 20, and 40 mm, respectively. Three replicates of each group were prepared for the reproducibility and accuracy of the experiments. Each filament has a width of 20 mm, while each layer's height measures 10 mm. Furthermore, there is a constant standoff distance of 10 mm between the nozzle head and filament, which is equivalent to the layer height. It should be noted that to simulate the practical engineering conditions, the built-in air cavity was manually sealed at the top and bottom after printing process, in preparation for the acoustics impedance tube tests.

Table 2. Characteristics particle sizes (μm) for river sand and crumb rubber.

| Characterised items | River sand (μm) | Crumb Rubber (μm) |
|---------------------|-----------------|-------------------|
| D ₁₀ | 107 | 1258 |
| D ₅₀ | 365 | 1929 |
| D ₉₀ | 1123 | 2940 |

4.3. Uniaxial compression tests

This study focuses on the examination of the compressive properties of 3DPRC, with a specific emphasis on

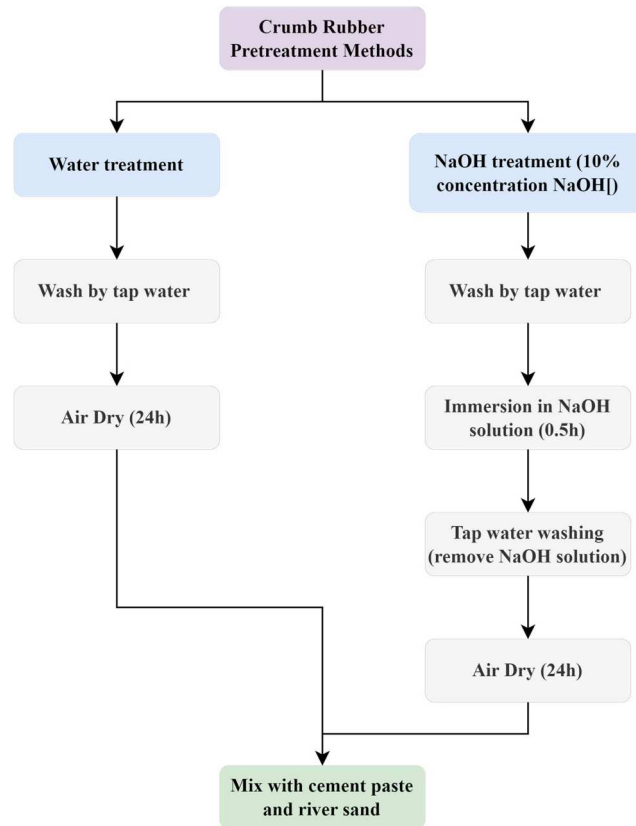


Figure 3. Workflow of the pretreatment process for crumb rubber granules before mixing.

assessing the impact of varying rubber content and different pretreatment conditions. Figure 7a illustrates 3DPC samples prepared for uniaxial compressive tests (UCTs), characterised by a cross-sectional dimension of 40 mm × 60 mm (W × H). This sample was 3D printed by employing a square nozzle with dimensions of 40 mm × 40 mm and subsequently subjected to a 28-day water curing process (under 23 °C). Then, cylindrical specimens measuring 25 mm in diameter and 50 mm in height were drilled from the X direction (printing

direction) and Z direction (layer deposition direction). For the UCTs, a 50kN Instron 5969 was employed as the loading device with a set loading rate of 0.18 mm/min. Compressive strain and axial displacement were measured using one strain gauge and two linear variable differential transformers (LVDTs). The detailed setup for the UCTs is demonstrated in Figure 7. To guarantee the accuracy of the measurement results, three samples were tested for specimens in both directions. To investigate the anisotropic compressive strengths

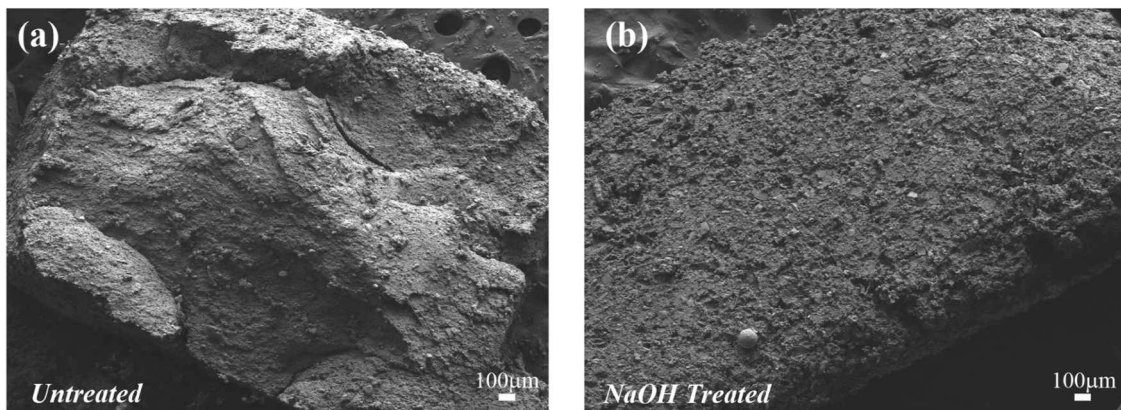


Figure 4. Micromorphology of crumb rubber granules: (a) Untreated rubber surface; (b) NaOH-treated rubber surface.

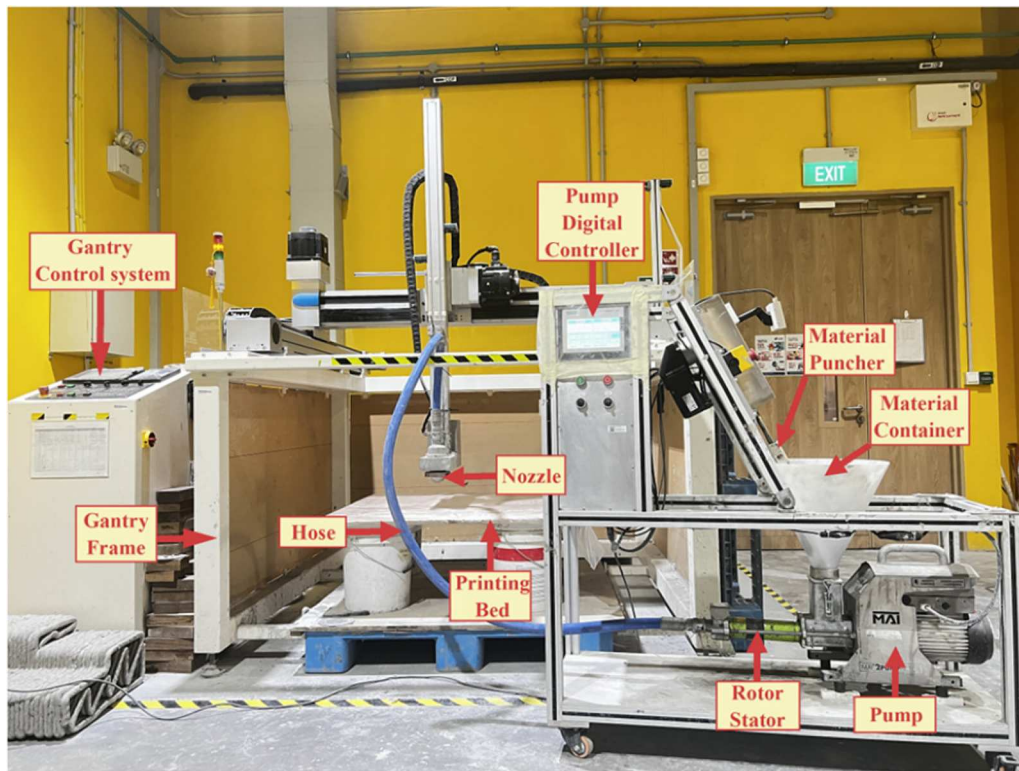


Figure 5. Set up of the 3D cementitious composites printing system.

for 3D printed concrete base on the printing path, only the loading in Z direction and Y direction are considered in this study. Based on the study conducted by Wolfs et al. [31], the loading directions X and Y can be considered equivalent and combined into one series. Apart from this, other research studying the anisotropic compressive strengths of 3D printed concrete in two loading directions can be found in [29, 32–34]. Therefore, it is appropriate to investigate the anisotropic compressive properties of 3DPC only in X and Z directions.

4.4. Acoustic insulation investigation

In this research, the sound insulation characteristics of 3DPRC blocks, encompassing sound absorption coefficients and sound transmission loss, are assessed following the ASTM E611-17 standard [25]. As illustrated in Figure 8, an impedance tube with a square cross-section was employed. Same instrument was reported in the study conducted by Crivoi et al. [35]. This tube features a loudspeaker positioned at one end, capable of emitting white noise generated and amplified through a Bruel & Kjaer (B&K) Type 2734-A power amplifier. Four B&K Type 4494-A 1/4-inch microphones, equipped with a LAN-XI Light 4-channel data acquisition (DAQ) module (as seen in Figure 8), were employed to measure the STL and SAC. A super clay

(Sykt. PPP Sdn. Bhd, Malaysia), known for its compacting properties, was employed to fill and seal any gaps between the uneven surface of the 3D printed cementitious composites specimens and the tube wall, which was crucial to prevent sound leakage during testing. A comparable sealing approach was employed to prevent undesired absorption, as demonstrated in the research conducted by Gourlay, Etienne, et al. [36]. For the transmission loss test, a tube with a length of 2.2 metres and a cross-sectional side size of 0.145 metres was employed. The distance between adjacent microphones was 0.05 metres for microphones 2 and 3, while the distance between microphone 2 and the edge of the specimen was 0.22 metres. In the acoustic absorption test, half of the tube was replaced by a short tube with a length of 0.21 metres, and the length of the tube was 1.31 metres.

4.5. Micro-structural analysis

Two characterisation experiments were conducted for micro-structural analysis which are Scanning Electron Microscopy (SEM) and X-ray micro-computed tomography (μ CT). In this study, 28-days-water-cured specimens were cut and fractured into small pieces with flat surfaces and coated with platinum under 20 mA currents for 120 s. After coating, the scanning of the specimens

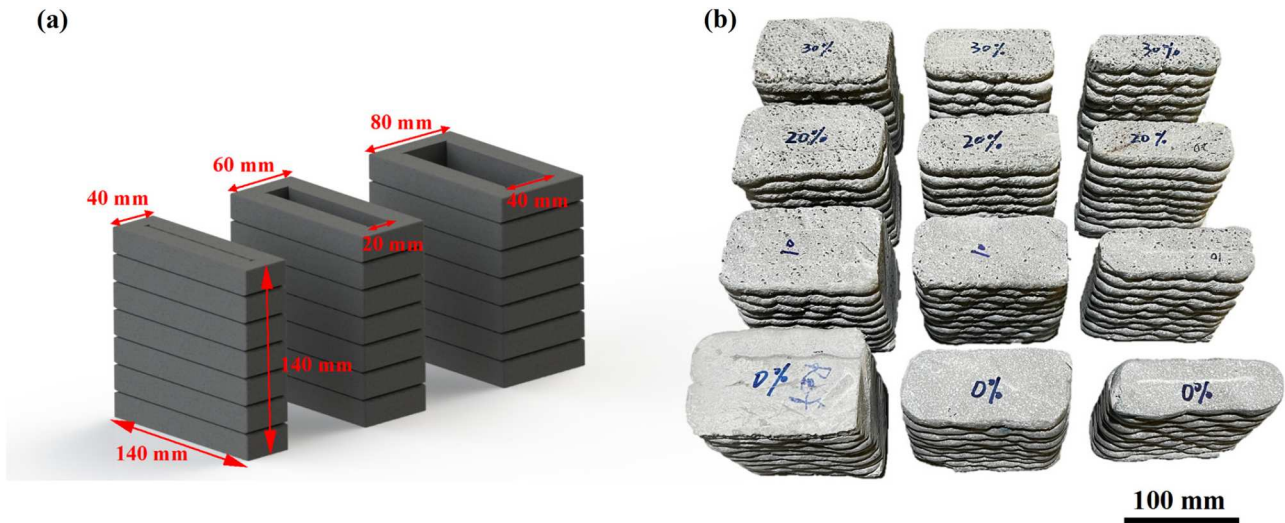


Figure 6. (a) Schematics of test specimens; (b) 3D printed rubberised cementitious composites blocks (built-in air cavity sealed at the top and bottom for the acoustic test).

was performed by FE-SEM device (JEOLJSM-6340F) under secondary electron mode with 10 kV accelerating voltage and 13 mm working distance. By utilising SEM scanning, the surface characteristics of rubber granules

and the interfacial gap between the rubber surface and cement matrix are studied in this work.

Characteristics of pore structure, such as porosity, pore size distribution, and pore morphology, in

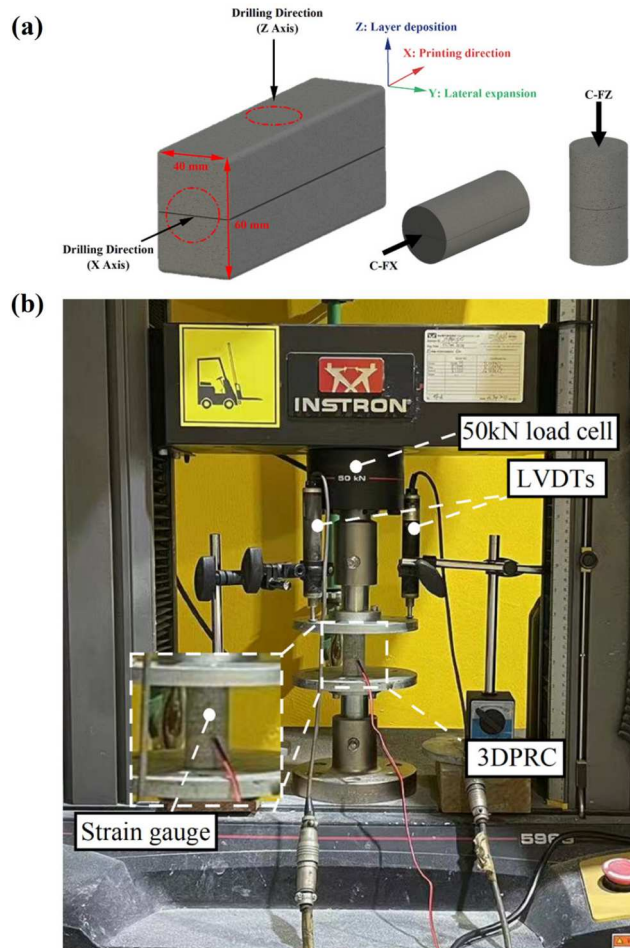


Figure 7. (a) 3D printed samples and (b) set up for the uniaxial compressive test.

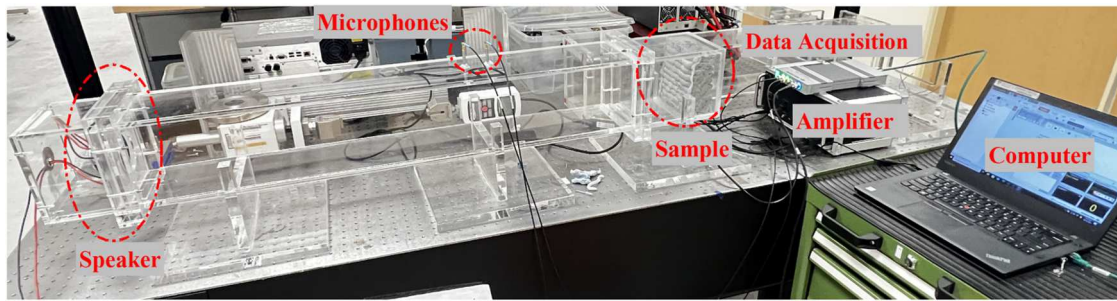


Figure 8. Demonstration of acoustic properties measurement instruments: impedance tube and accessories.

cementitious materials are significant for studying its acoustic and mechanical properties. Nondestructive evaluation of the microstructure within the specimen was conducted using Bruker's Skyscan 1173 μ CT scanner. In this investigation, cylindrical samples with a diameter of 25 mm and a height of 50 mm, drilled from the 3DPRC blocks, were prepared for μ CT scan. Subsequently, a total of 900 two-dimensional projection images were acquired. The acquisition parameters encompassed an exposure time of 1000 ms, X-ray energy settings of 70 kV, and an anode current of 160 μ A, all implemented with a voxel size resolution of 48 μ m. Notably, an attenuating brass filter was judiciously positioned in the path of the X-ray source to ameliorate the inherent noise levels. After scanning, the 2D projection images were imported into the slicing software, NRecon, and 1000 slices uniformly spaced in a consistent manner were then generated. Following the phase, the 2D images were transmuted into a 3D voxel-based morphometry model, facilitating the subsequent evaluation of pore parameters. Finally, the volumes, porosity, orientation characteristics, and 3D visualisation of the pores can be obtained with the assistance of Avizo 3D software, which supports the analysis of the acoustic absorption mechanisms in 3DPRC.

5. Experimental results

5.1. Rheological properties

The results elaboration and discussion of the rheological properties of 3DPRC materials are included in section 1.2 of supplementary information. The relationship between rheological properties and rubber replacement ratio in 3DPRC is also illustrated in Figure S2 in the supplementary information.

5.2. Compressive properties

The UCTs provided insights into the 28-day compressive strength and stress–strain relationships of 3DPRC with

varying CR content and pretreatment conditions, as illustrated in Figure 9. To investigate the effects of CR content on the mechanical properties (strength and deformation) of 3DPRC, Figure 9a presents typical compressive stress–strain curves for 10% CR, 20% CR, and 30% CR (X and Z Direction) and the control group (Control-X and Control-Z). These curves exhibit two distinct behavioural patterns. A trend for the stress to increase linearly until reaching peaks and then fail can be observed in specimens 10% CR, 20% CR and Control. However, compared to Control group, the addition of CR results in reduced deflection in the elastic region and lower peak stress, indicating a more brittle material behaviour in 3DPC and 3DPRC with lower CR content. Nevertheless, the stress–strain curve of 3DPRC becomes nonlinear with increased CR content. Both 30% CR-X and 30% CR-Z demonstrate yielding and generates plastic energy as cracks develop after peak stress. In this case, the behaviour of the stress–strain curve of 30% CR is similar to the behaviour of tough material. Hence, 3DPRC with higher CR content exhibits increased toughness, as evidenced by this altered stress–strain behaviour. It should be noted that Figure 9a indicates the effect of CR content on the stress–strain behaviour, instead of studying the pretreatment effects. According to the study proposed by Najim et al. [37], it can be found that different pretreatment methods of the crumb rubber only affect the value of peak value of the stress–strain curve, but have insignificant effects on the failure pattern and toughness of the 3DPRC. Therefore, only the NaOH treated group was presented and studied. Based on Figure 9b, it can be concluded that the compressive strength of the 3DPRC in both directions visibly decreases with increasing the CR content. This outcome aligns with expectations, as the incorporation of crumb rubber (CR) introduces greater discontinuity in the cement paste. This is caused by weak bonding at the interfacial transition zone (ITZ) and reduced stiffness resulting from the partial replacement of sand particles with CR granules. The reduced stiffness of rubber granules compared to

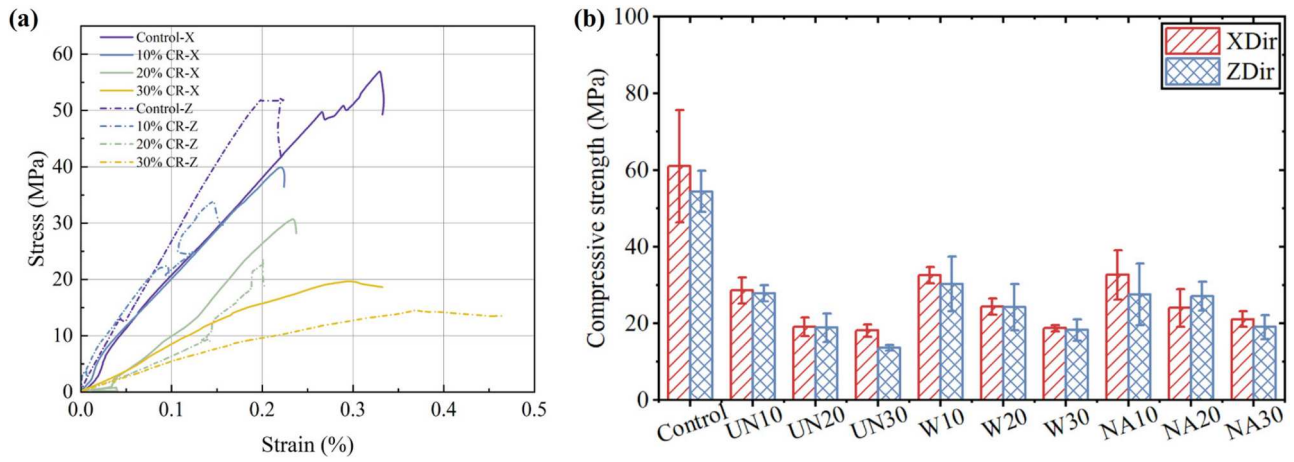


Figure 9. (a) Relationship between stress and strain for 3DPRC with different CR content; (b) compressive strengths of 3DPRC with different CR content and pretreatment conditions.

the adjacent cement matrix and fine aggregate causes these particles to function as soft inclusions. This difference in stiffness leads to stress concentration around the rubber particles, consequently reducing the overall mechanical performance of the composite. Based on these experimental results, the impacts of crumb rubber content on the compressive strength will be quantitatively analyzed in Section 6.3 and a model will be proposed. Notably, considering the anisotropic compressive properties of 3DPRC, the compressive strength of the specimens loaded in X direction, such as Control-X (61.1 ± 7.3 MPa), UN10-X (28.6 ± 1.7 MPa), W10-X (32.6 ± 1.1 MPa), NA10-X (32.7 ± 3.2 MPa), are 12.1%, 2.5%, 7.3%, 18.6% larger than those of specimens loaded in Z direction, respectively. The variation in compressive strength due to loading direction in 3DPRC is influenced by the tri-axial spheroid-shaped air voids within the interlayer region, which is stretched from circle pores during the printing process [22], and stress concentration along the pore boundaries, which respond differently to the direction of applied load. Stress concentration along the pore boundaries is greater in specimens subjected to loading in the Z-direction compared to those loaded in the X-direction. This increased stress concentration contributes to a reduction in compressive strength in the Z-direction-loaded specimens.

The impact of CR pretreatment on compressive strength was also investigated. It was observed that 3DPRC samples with modified CR, subjected to various pretreatment methods, exhibited varying degrees of strength enhancement. Specifically, UN10 showed compressive strengths 13.8% and 14.4% lower than those with W10 and NA10, respectively. This pattern persisted across other CR replacement levels, as evident in

comparisons of UN20, W20, NA20, and UN30, W30, NA30. Finally, it can be summarised that 3DPRC containing CR treated by NaOH solution shows optimum compressive strength compared to those treated by water or without treatment. Furthermore, a detailed analysis of the reasons from a microscopic view behind the enhanced compressive performance of specimens treated with NaOH is provided in Section 5.2.

5.3. SEM analysis

To further explain how pretreatment conditions affect the compressive strength of 3DPRC at the microstructural level, SEM images of the interface between treated/untreated CR particles and cement paste were analyzed, as shown in Figure 10. The interface with untreated CR, shown in Figure 10a, presents a large gap, indicating poor adhesion and consequently weaker macro-level mechanical properties. This can be attributed to the surface hydrophobicity, smooth surface, and lack of chemical bonds between rubber surface and cement paste. As for the 3DPRC with water-treated CR (Figure 10c), a smaller gap is observed, suggesting improved adhesion due to a cleaner rubber surface. The water washing of the crumb rubber can remove the rubber powder from the surface, which can enhance the adhesion between the cement paste and the rubber surface. Most notably, Figure 10d shows that NaOH pretreatment significantly densifies the interfacial microstructure. This is attributed to the ability of NaOH to convert zinc stearate, a compound contributing to the hydrophobic characteristics of the rubber surface, into a soluble form of sodium stearate. This transformation allows the sodium stearate to be removed through water washing. The removal of

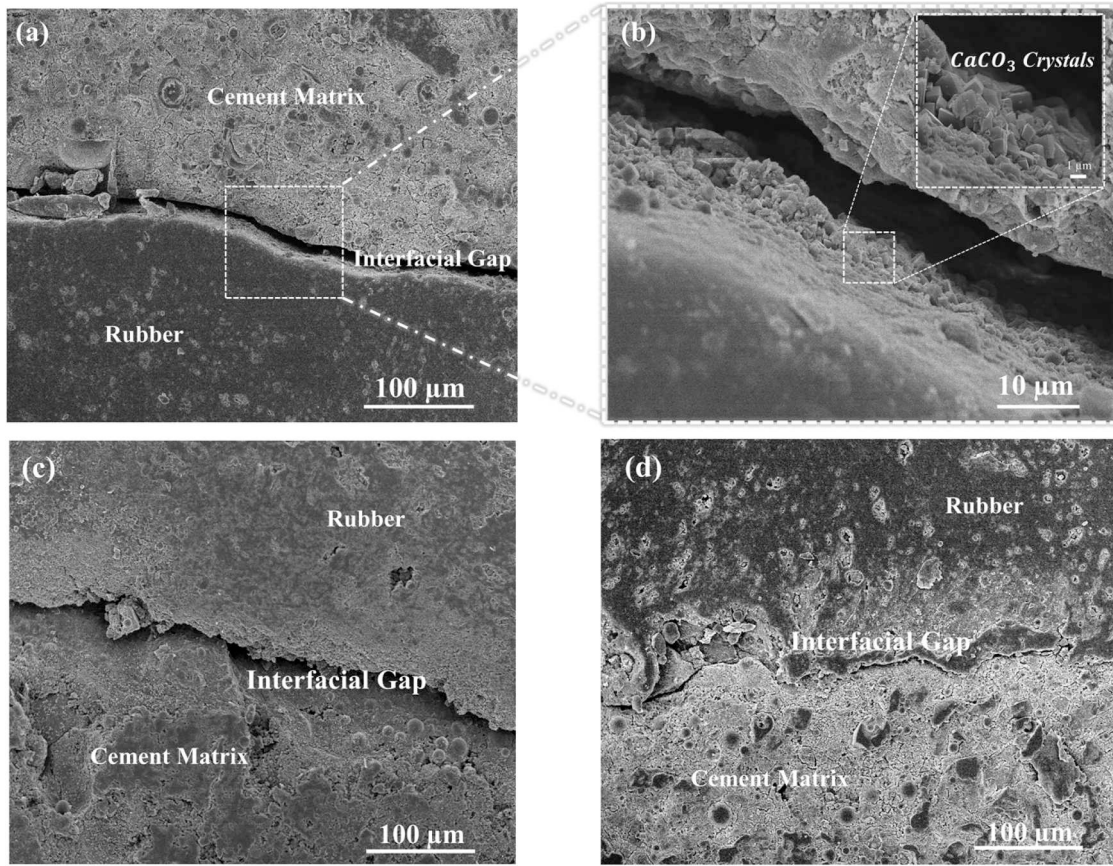


Figure 10. SEM images of the interfacial region of 3DPRC with distinct rubber surface treated conditions: (a) untreated CR with 250 times magnification; (b) untreated CR with 2000 and 10000 times magnification; (c) water treated CR; (d) NaOH treated CR.

rubber powder and zinc stearate results in a rough and porous surface, making it scraggy and consequently enhancing the cohesion between rubber particles and cement paste [30]. This microscopic analysis aids in analyzing how different pretreatment methods influence the bonding strength between CR particles and cement paste, thereby impacting the overall compressive strength of 3DPRC.

5.4. Acoustic absorption characteristics

To assess the impacts of incorporating CR granules and built-in cavities within the 3DPRC on the acoustic absorption properties, experiments were conducted to measure SAC at various CR content levels and cavity thicknesses. The SAC curves, covering the frequency range from 100 Hz to 1000 Hz, are depicted in Figure 11. The SAC peak values for 3DPRC with 10%, 20%, and 30% CR content exhibited significant increases, reaching 0.315, 0.524, and 0.733, respectively, compared to the control group with a SAC value of 0.248, as illustrated in Figure 11 (a). Additionally, the NRC was computed according to Eq. (3) for each group to provide a

comprehensive assessment of sound absorption capabilities. The findings suggest that the introduction of crumb rubber granules enhances the efficiency of sound absorption characteristics.

$$NRC = (\alpha_{250} + \alpha_{500} + \alpha_{1000})/3 \quad (3)$$

where α_{250} , α_{500} , α_{1000} represent the SAC at the four one-third octave bands centred at of 250, 500, and 1000 Hz, respectively. Owing to the constraints imposed by the size limitation of the impedance tube, SAC values exceeding 1100 Hz are deemed unreliable due to the limitation of the cross-section size of the tube and, accordingly, have been excluded from the computation of NRC.

Furthermore, it is evident that the peaks in the SAC curves exhibit a shift towards higher frequencies as the proportion of CR content increases. Specifically, the frequency associated with the peak in the SAC curves for 10% CR, 20% CR, and 30% CR shifted to 334, 431, and 483 Hz, respectively, compared to the control group for the acoustic test (267 Hz). Additionally, the trend of the SAC curves remains consistent for specimens with different CR content, which aligns with the acoustic absorption behaviour of porous and lightweight

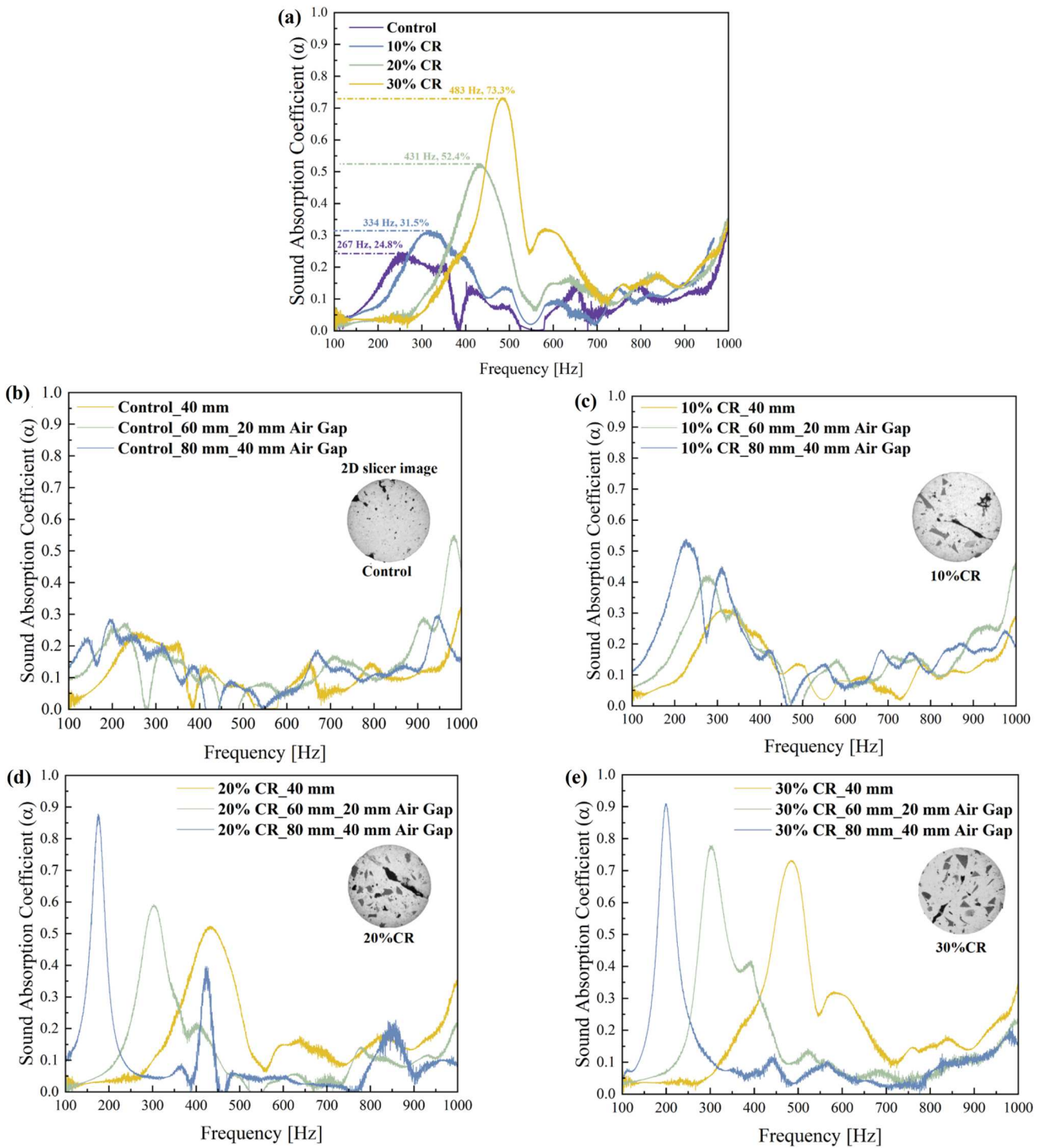


Figure 11. Measured SAC in 3D printed rubberised cementitious composites: effects of rubber content and cavity thickness.

cementitious materials [38]. Furthermore, the sound absorption curve bandwidth, which is defined as the frequency range that exceeds the absorption efficiency of 0.2, significantly increases as the CR content increases. Specifically, the sound bandwidth for 10%CR, 20%CR, and 30%CR exhibited significant increases, which are 151, 170, and 294 Hz, respectively, compared to the control group with a SAC value of 103 Hz. This

phenomenon signifies that an increase in the CR content increases the frequency and frequency range of sound waves which can be efficiently absorbed by 3DPRC.

Apart from the investigation of the impact of materials on the sound absorption properties of 3DPC, this study also initiates a preliminary exploration of the structural impact on sound absorption performance by

introducing built-in cavities within 3DPRC blocks. As depicted in Figure 11b to e, SAC was measured for four different specimen groups, each characterised by distinct air gap thicknesses. The 2D slicer images of 3DPRC containing 10%, 20%, and 30% crumb rubber are displayed in the upper right corner of each figure. These images help visualise the quantity, geometry, and distribution of pores within the material. For the control group without the CR, as the built-in cavity thickness increases, a slight improvement in the peak value of SAC can be observed in Figure 11b. A similar trend is observed in the 10% CR, 20% CR, and 30% CR groups. Notably, in the 10% CR group, the SAC experiences a substantial increase, rising from 0.32–0.42 when the cavity thickness increases from 0 to 20 mm, and further to 0.54 as the thickness extends from 20 mm to 40 mm. Moreover, it is observed that the acoustic absorption peak gradually shifts to lower frequency ranges with increasing built-in cavity thickness. Particularly, the SAC for specimens with a 40 mm cavity in the 20% CR group reaches 0.87 at an exceptionally low frequency of 175 Hz. This result verified the positive influence of built-in cavities on the sound absorption performance for sound energy at longer wavelengths (lower frequencies).

5.5. Acoustic insulation behaviours of 3DPRC

In addition to examining the sound absorption properties of 3DPC, it is crucial to consider the effects of CR replacement ratio and the thickness of built-in air gaps on STL, which plays a significant role in sound insulation assessment. STL is defined as the ratio of sound pressure at the rear to the front surface of a porous specimen when sound waves propagate through it. Measurements were conducted utilising the two-load method, as described in Section 3.

Figure 12 illustrates the experimental (STL) over a frequency range of 50 Hz to 1100 Hz for 3DPRC with varying rubber content and air cavity thickness. In general, the polynomial fitted curves for STL across all specimens exhibit a common trend of increasing values at lower frequencies and declining near 1000 Hz, ranging from 2 dB to 25 dB. Notably, as observed in Figure 12a, the average STL indices for composites containing 10% CR, 20% CR, and 30% CR are 15.3, 18.4, and 16.8 dB, respectively, which is higher than that of plain mortar (11.4 dB). This significant improvement can be attributed to the enhanced viscoelastic properties of CR when compared to natural aggregates, as explained by Zhao et al. [39]. However, it is worth noting that the STL indices of 30% CR are observed to be smaller than those of 20% CR, which deviates from

the mechanisms discussed above. This phenomenon can be explained by considering the increased porosity and decreased mass density of 3DPC with higher CR replacement ratios, allowing easier sound propagation through air voids and thereby reducing STL [40]. Therefore, it can be summarised that the sound insulation properties of 3DPC at low frequencies depend on the damping properties of the material, mass density, and porosity. Incorporating CR at 10% and 20% primarily boosts sound insulation properties through damping effects, overshadowing air void content. However, at higher rubber replacement levels, like 30%, air void content assumes greater significance, leading to a decrease in STL.

STL fitting curves for specimens featuring varying thicknesses of built-in air gaps (CR_60 mm and CR_80 mm) are shown in Figure 12 (b–e). It is evident that, for the control group, 20% CR, and 30% CR specimens, the average STL of specimens with 40 mm built-in air gap (CR_80 mm) increased by 68.9%, 25.8%, and 12.6% respectively, compared to specimens without air gaps. Additionally, it is worth highlighting that, for all specimens featuring built-in air gaps, the fitted STL curves demonstrate an upward and then downward trend within 50–1100 Hz. The peaks of the curves for specimens with 20 mm air gaps are concentrated within 900–1000 Hz, while for specimens with 40 mm air gaps, the maxima shift to 700–800 Hz. Furthermore, at 1100 Hz, STL indices for 40 mm gap specimens are lower than those without gaps, particularly in crumb rubber-containing specimens.

It is well-established that increased sample thickness enhances sound insulation properties due to the greater mass per unit area. Koruk et al.'s study [41] found STL linearly increases with thickness across frequencies in specimens of 10, 12.5, 15, and 20 mm. In our research, varying thicknesses of specimens are achieved by introducing different thicknesses of air gaps within the 3D-printed cementitious composites blocks. Furthermore, based on the analysis of the experimental results, it can be concluded that the thickness of the air gap within the structure significantly enhances the sound insulation performance of 3DPC, which is aligned with trends observed in the research conducted by Zhou et al. [42]. This enhancement can be attributed to the air gap acting as an elastic layer, promoting sound wave attenuation through multi-reflection in the mass-air-mass structure. Furthermore, the incorporation of built-in air gaps within the structure, facilitated through the utilisation of 3D printing technology, not only enhances sound insulation properties but also saves material without compromising sound insulation capabilities.

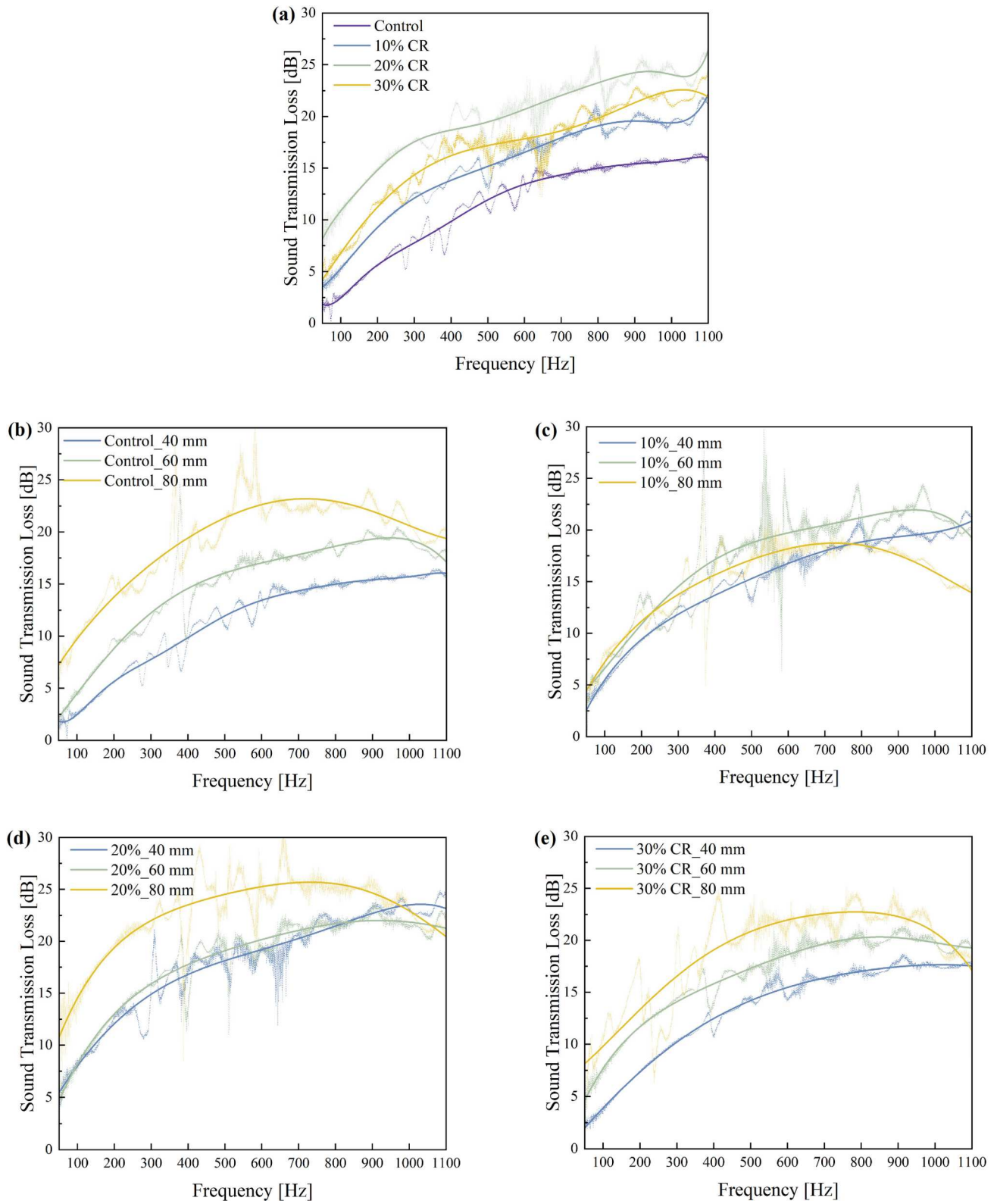


Figure 12. Experimental-based sound transmission loss results with various rubber replacement ratios and distinct built-in air gap thickness.

6. Discussions

6.1. Acoustic absorption mechanisms of 3DPRC with the aid of μ -CT

Based on the experimental result, further explanation of the specific sound absorption mechanisms unique to 3D printed cementitious composites compared to conventional cast concrete is essential. In the impedance tube test, a normal-incident acoustic plane wave partially reflects off the surface of the 3DPC block, while the remainder penetrates through the open pores of the rigid frame porous structure. Partial energy of the penetrating acoustic wave is dissipated in the elongated open pore, while the rest is emitted to the back of the block. Figure 13 shows an elongated open pore morphology in the 3DPC, resembling an interconnected microscopic cavity. Each resonator, comprising a closed spherical cavity with a hard interior and a narrow aperture to the external environment, absorbs sound waves with low frequency effectively. A comparable correlation between the pores containing aperture-cavity unit and Helmholtz resonator was also proposed by Wang et al. [43]. Three sound absorption mechanisms are engaged within the elongated open pore, as depicted in Figure 13: (1) viscous effect, (2) thermal effect, and (3) material damping effect [44]. The viscous dissipation effect occurs as sound waves induce vibrations and friction in air molecules at the specimen's surface and within the aperture-cavity structure. Resonance happens when the excitation frequency matches the natural acoustic resonance frequency of this structure, significantly enhancing sound absorption at specific frequencies, as shown by peaks of the SAC curves in Figure 11. Additionally, thermal-elastic damping from isothermal heat transfer due to wave-wall collisions dissipates the acoustical energy into heat. Material damping, especially for rubber granules with high damping ratios, further attenuates sound wave energy by dispersing vibrations.

The experimental findings demonstrate that 3DPRC exhibits effective sound absorption performance, particularly in low-frequency ranges, which aligns with prior studies by Sambucci et al. [45] and Asdrubali et al. [46]. Table 3 indicates the NRC of both 3DPC and conventional cast concrete, where the preferable sound attenuation performance of 3DPC compared to cast concrete can be observed. For instance, Wang et al. [9] discovered that a 30% replacement of CR yields the most favourable sound attenuation properties ($\text{NRC} = 0.17$). Similar findings have been reported by Ling et al. [10] and Sukontasukkul [11], where the optimal NRC for rubberised cast concrete in these works are 0.12 and 0.19, respectively.

Notably, it can be calculated that the optimal NRC of 3DPRC with 30% CR content in this study is 0.35. Additionally, the primary frequency range (the frequency range corresponds to the peak of SAC curves) for 3DPC is concentrated between 250 and 500 Hz. This finding aligns with the primary frequency range, which is concentrated in the low-frequency range, reported by Sambucci et al. [45]. However, for cast concrete, the primary frequency is centred at a higher domain around 1000 Hz, which is not preferable in insulating the noise generated by transportation. Herein it can be demonstrated that the acoustic absorption performance of rubberised 3DPC is better when compared to conventional cast concrete in the aspects of higher NRC value and lower primary frequency.

To further explain the enhanced sound absorption performance of 3DPRC, it is significant to investigate the microscopic characteristics of the pores generated within the concrete due to different fabrication processes compared to cast concrete. The overall porosity of the cement matrix is observed to increase as the CR content rises. This phenomenon, as demonstrated by Mohammed et al. [40] is attributed to the entrapment of air at the interfacial region between the cement paste and rubber (aggregate) surface, contributing to higher porosity. It is significant to note that cast concrete utilises compaction to minimise air voids, whereas 3D printing does not incorporate this step, leading to more entrapped air when the same quantity of rubber is applied. The 2D micro-CT image in Figure 14c and the images of SEM in Figure 10 both depict the presence of entrapped voids within the interfacial zone, facilitated by the low hydraulic conductivity and smooth surface of the rubber particles [30].

Furthermore, open pores significantly contribute to sound energy absorption in concrete due to their continuous communication channel with the external surface. Conversely, closed pores, isolated from neighbouring pores, primarily affect macroscopic concrete properties such as thermal conductivity, bulk density, and mechanical strength, playing a lesser role in sound absorption [44]. Therein, it can be concluded that materials with a higher volume ratio of open pores exhibit more effective sound energy absorption. The ratio of open pore volume and the ratio of closed pore to overall pore volume for both 3DPC and cast concrete are shown in Table 4. It is evident that in all 3DPC groups, the percentages of the open pore to total pore volume are 50.9%, 68.8%, 56.6%, and 57.4%, respectively. However, in cast concrete, the ratio of open pore accounts for only 34.4%, which means the volume of closed pore in the concrete matrix is larger and its ability of energy attenuation is weak. Notably, this

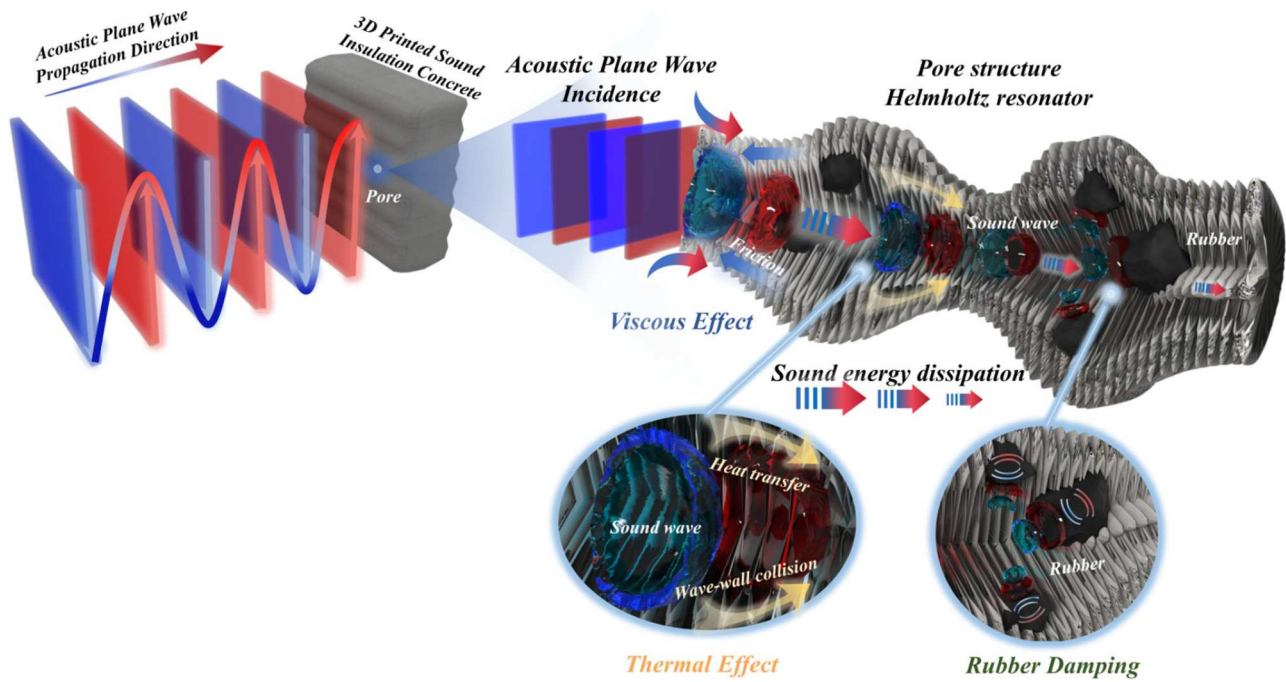


Figure 13. Schematic illustration of acoustic energy dissipation mechanisms (viscous effect; thermal effect; material damping) in the pore structure of a 3D-printed rubberised cementitious block, from macroscopic (left) to microscopic (right) levels.

finding aligns with the study conducted by Mukhame-trakhimov et al. [47].

The experimental results concerning the SAC for 3DPRC necessitate a comparative analysis with other sound-absorbing and traditional construction materials. As detailed in Table 5, plain concrete walls exhibit robust mechanical strength but are characterised by relatively poor sound absorption performance, with an SAC ranging from 0.03–0.1. In contrast, lightweight cast concretes such as hemp concrete, cellular concrete, rubberised concrete, and foam glass concrete demonstrate better sound absorption behaviours compared to plain cast concrete.

Commercial sound-absorbing materials, including acoustic foam, mineral wool, cork, and other fibrous materials, exhibit notably higher sound absorption efficiency compared to cementitious materials. However, these commercial sound-absorbing materials generally lack the load-bearing capacity that cementitious materials provide. Remarkably, 3DPRC, achieving an optimal NRC of 0.354, shows enhanced sound absorption

performance relative to traditional cast cementitious materials and displays better mechanical behaviours than commercial sound-absorbing materials. Consequently, 3DPRC emerges as a multifunctional material, making it highly suitable for applications that require both sound absorption and structural integrity within the construction industry. This dual functionality allows 3DPRC to offer a balanced solution, meeting both acoustic and structural requirements in building applications.

Kruger et al. [22] indicated that intralayer voids within 3DPC exhibit elongated shapes along the printing direction (X), attributed to the dragging effect of the nozzle head during the printing process. In contrast to the isolated and spherical voids found in cast concrete, as depicted in Figure 14a, the morphology of elongated pores within 3DPC can be observed in 2D micro-CT images (Figure 14c) and the 3D reconstruction model (Figure 14d). As mentioned, pores within the cement matrix can be treated as Helmholtz resonators when considering the sound attenuation effect. Isolated spherical pores in cast concrete,

Table 3. Comparison of the optimal NRC and Primary Frequency Range of 3DPRC with cast rubberised concrete.

| Group | 3D Printed rubberised cementitious composites (This study) | | Cast Concrete [9] 30% CR | Cast Concrete [10] 30% CR | Cast Concrete [11] 20% CR | 3DPC [45] 100% CR |
|---|--|------------|-----------------------------|------------------------------|------------------------------|----------------------|
| | 20% CR | 30% CR | | | | |
| Optimal Noise Reduction Coefficient (NRC) | 0.22 | 0.36 | 0.17 | 0.12 | 0.19 | 0.44 |
| Primary frequency range (Hz) | 300-350 Hz | 450-500 Hz | 1000 Hz | 500-1500 Hz | 1000 Hz | 500 Hz |

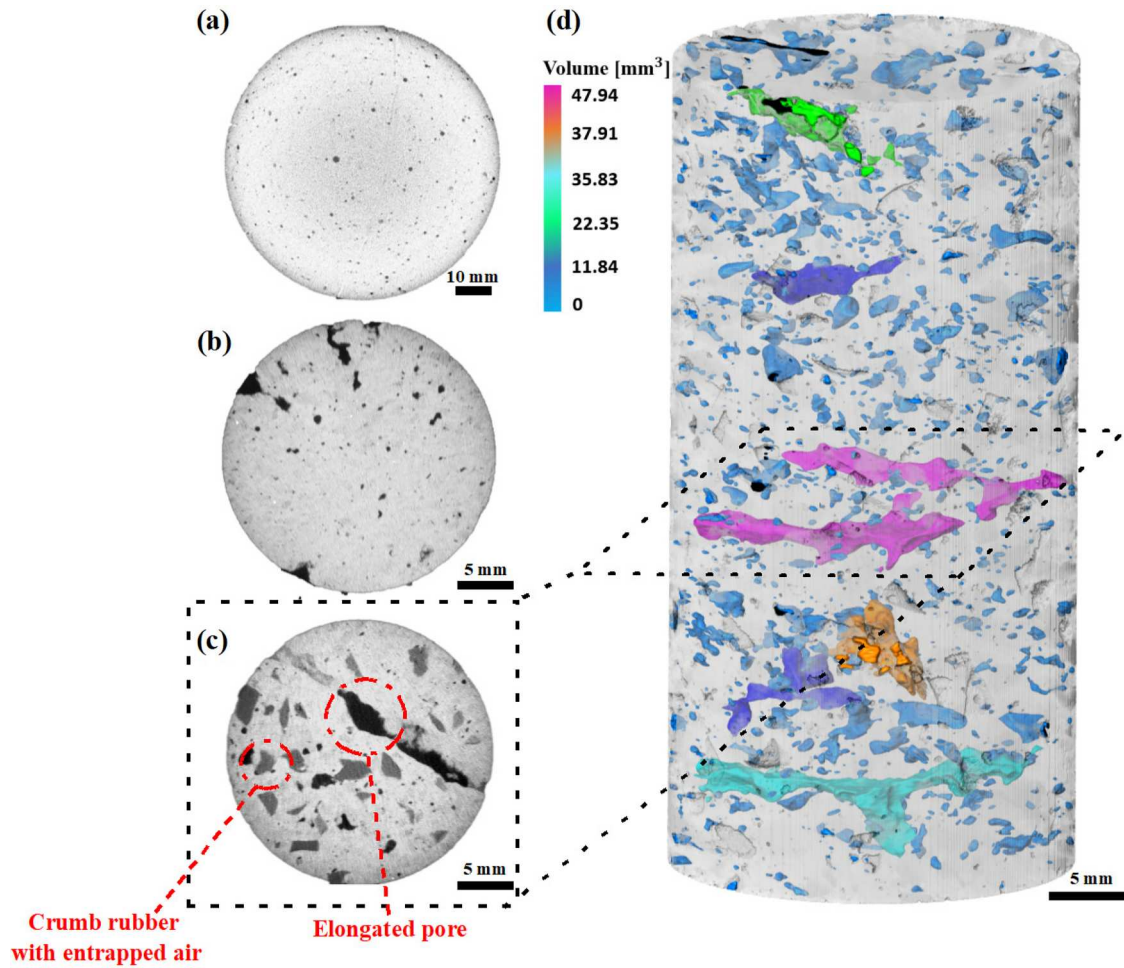


Figure 14. Schematic μ -CT scan results illustrating pore characteristics: (a) slicer image of conventional cast concrete; (b) 3D printed specimen (control group); (c) 3D printed specimen (20% CR); (d) 3D rendering model (20% CR) indicating voids geometry, position, volume, and distribution.

serving as discrete Helmholtz resonators, have a limited impact on acoustic energy dissipation. Nevertheless, the interconnected, elongated pores in 3DPC, treated as a chain of Helmholtz resonators, facilitate sustained sound energy attenuation and thus improve the acoustic absorption of 3DPC. Furthermore, the orientation of elongated pores in the X-Y plane relative to the direction of incoming sound waves significantly impacts the sound absorption properties. As noted by Huang et al. [54], sound waves that approach perpendicularly to the channel orientation are partially reflected. In contrast, when channels align parallel to the sound transmission path, the waves transmit with minimal loss. However, obliquely oriented channels increase the travel path of the sound waves, causing multiple reflections and increased air friction, which leads to greater energy dissipation. This study employs these principles to analyze the transmission of sound waves through the elongated pores of 3DPRC.

Using 3D reconstruction technology and Avizo commercial software, the orientation of each pore relative to incoming sound waves has been quantitatively assessed. Figure 15 illustrates the distribution of pore orientations ranging from 0° to 90° , where 0° represents pores oriented perpendicular to the sound incidence direction and 90° represents pores parallel to the sound's approach. It is observed that the proportion of oblique pores increases with the crumb rubber content in the 3DPRC, except in the control group. A comparison of the oblique pore proportions with the sound absorption performance of the 10% CR, 20% CR, and 30% CR groups indicates a positive correlation between the number of oblique pores and sound absorption properties. However, due to the limited number of experiments, only a qualitative relationship between the ratio of oblique pores and the sound absorption of 3DPRC has been proposed. The high proportion of oblique pores but the low sound absorption coefficient in the control group is caused by the low total porosity. However, it

Table 4. Pore characteristics and input data for simulation of 3D printed rubberised cementitious composites.

| Characterised items | Porosity (ratio of Open pore/ Closed pore) | Air Flow Resistivity ($\text{Pa} \cdot \text{s}/\text{m}^2$) (Eq. 8) | Tortuosity (Eq. 7) | Standard Deviation of Pore size | Noise Reduction Coefficient (NRC) (Eq. 3) | Density (kg/m^3) |
|---------------------|---|---|-----------------------|------------------------------------|--|---------------------------------------|
| Control | 2.78% (50.90%/49.10%) | 228332 | 18.49 | 0.52 | 0.208 | 2032 |
| 10% CR | 3.30% (68.80%/31.20%) | 107697 | 15.65 | 0.79 | 0.213 | 1981 |
| 20% CR | 4.95% (56.60%/43.40%) | 52368 | 8.83 | 0.53 | 0.223 | 1934 |
| 30% CR | 7.60% (57.40%/42.60%) | 28423 | 7.08 | 0.67 | 0.354 | 1904 |
| Cast concrete | 1.49% (34.40%/65.60%) | - | - | - | - | - |

proves the presence of elongated oblique pores in 3D printed concrete, which offers better sound attenuation effects for 3D printed concrete compared to cast concrete, where pores are predominantly spherical.

6.2. Simulation validation with experimental measurements

To further verify the acoustic absorption properties of 3DPRC, emphasis was placed on the varying content of CR and the thickness of the integrated cavities. A 3D Finite Element Analysis (FEA) model was formulated using the Pressure Acoustic Module within COMSOL Multiphysics. The numerical model is built with two distinct domains: (1) the ambient sound pressure field, which incorporates a port situated at the tube's extremity to introduce a normal-incidence sound wave; and (2) the porous acoustic domain. This domain encompasses the porous concrete region, modelled using the Attenborough poroacoustic framework, in tandem with the air domain symbolising the built-in air gap. The Attenborough model, an augmentation of the Zwikker-Kosten model, is a semi-empirical approach with four input parameters, utilised to determine the acoustic impedance of porous material. The equivalent density and bulk modulus of the porous materials are defined as:

$$\rho = \frac{\rho_f}{\varepsilon_p} \frac{\tau_\infty}{1 - \frac{2}{s' \sqrt{-i} J_0(s' \sqrt{\text{Pr}} \sqrt{-i})} \frac{J_1(s' \sqrt{\text{Pr}} \sqrt{-i})}{J_0(s' \sqrt{\text{Pr}} \sqrt{-i})}} \quad (4)$$

$$K = \frac{\gamma P_A}{\varepsilon_p} \frac{1}{1 - (\gamma - 1) \frac{2}{s' \sqrt{\text{Pr}} \sqrt{-i} J_0(s' \sqrt{\text{Pr}} \sqrt{-i})} \frac{J_1(s' \sqrt{\text{Pr}} \sqrt{-i})}{J_0(s' \sqrt{\text{Pr}} \sqrt{-i})}} \text{Pr} = \frac{C_p \mu}{k} \quad (5)$$

Table 5. The sound absorption coefficient of construction materials and commercial sound absorbing materials.

| Type of Materials | Noise Reduction Coefficient | Reference |
|--------------------------------|-----------------------------|-----------|
| Plain concrete wall | 0.03-0.1 | [48] |
| Light weight concrete | 0.12-0.3 | [49] |
| 3D printed rubberised concrete | 0.354 | |
| Acoustic foam | 0.4-0.8 | [50] |
| Mineral wool | 0.36-0.75 | [51] |
| Fibrous material | 0.2-0.75 | [52] |
| Cork | 0.2-0.4 | [53] |

where P_A denotes the ambient pressure, ρ_f represents the fluid density, γ is the ratio of specific heat, Pr is the Prandtl number, C_p is the heat capacity at constant pressure, and k is the coefficient of thermal conduction. J_0 and J_1 are Bessel functions of the first kind. The variable s' is anisotropy factor is derived from other material parameters:

$$s' = b \sqrt{\frac{8\omega\rho_f\tau_\infty}{\varepsilon_p R_f}} \quad (6)$$

where ω denotes the angular frequency. The four parameters required to input are the porosity ε_p , the tortuosity τ_∞ , flow resistivity R_f , and the fitting parameter b . The fitting parameter b is related to the anisotropy of the pores and tabulated for certain well-defined pore cross-sections.

Among the four input parameters, the porosity of the specimen is derived from the micro-CT analysis, with specific values for each group delineated in Table 4. Given the experimentally determined porosity, tortuosity, which pertains to the pore orientation in relation to the direction of sound wave propagation, is computed in accordance with Equation 7 as proposed by Horoshenkov et al. [55].

$$\tau_\infty = 1 + \frac{1 - \varepsilon_p}{2\varepsilon_p} \quad (7)$$

Furthermore, the flow resistivity shown in Table 4 is defined as the real part of the ratio between the pressure drop and the flow velocity through a layer of material of unit thickness, which can be calculated from Eq. (8) proposed by Horoshenkov et al. [55].

$$R_f = \frac{400(1 - \varepsilon_p)^2(1 + \varepsilon_p)^5 \mu}{\varepsilon_p D^2} \quad (8)$$

In this equation, μ signifies the dynamic viscosity of air, while D denotes the characteristic dimension of aggregate particles. Notably, to ensure prediction precision, the effective particle size-integrating value of D_{90} from both crumb rubber and sand are utilised as D in the equation. Table 4 lists the specific values of the tortuosity and resistivity for all groups. Incorporate with the material properties such as density and Young's modulus of 3DPC, the four parameters would be inputted for the numerical analysis of sound absorption

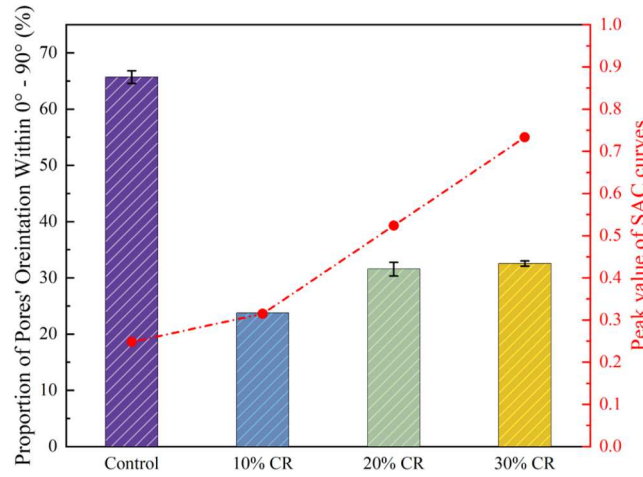


Figure 15. The proportion of elongated pore orientations within the 0° to 90° range concerning the direction of incident sound waves, analyzed by commercial software Avizo.

performance. The pressure reflection coefficient can then be calculated by determining the ratio of P_{scat} and P_{inc} , where the scattered pressure (P_{scat}) and the incident pressure (P_{inc}) are obtained from the pressure produced and received at the port. Therein, the sound absorption coefficient (α) in the aspect of frequency up to 1000 Hz is defined as follows.

$$\alpha = 1 - |R|^2 \quad (9)$$

As for the boundary conditions, sound hard boundaries are applied on lateral boundaries as well as at the tube's terminus, reflecting the practical scenario. The port boundary condition, serving as the excitation source, is implemented at the end of the tube to initiate normal incident sound waves. A finer tetrahedral mesh, ranging from a minimum mesh element size of 5.2 mm to a maximum of 71.5 mm, is employed for this investigation.

Based on the acoustic and non-acoustic parameters of the 3DPRC, the numerically simulated SAC spectrums are illustrated in Figure 16a and compared with experimental results in Figure 16b. Discrepancies between peak values and their corresponding SAC frequencies from experimental and simulated data are quantified. For the control group, 10% CR, 20% CR, and 30% CR, the deviations are 21.77%, 2.86%, 0.10%, and 0.04%, respectively, suggesting commendable concordance between experimental and simulated SAC values. It can be noted that the higher the crumb rubber content, the better the fit of the numerical simulation results to the experimental ones. Furthermore, a highly analogous trend in SAC curves from both simulation and experimental results is discernible in the 100-1000 Hz spectrum. In the simulations examining air cavity thickness effects, specimens incorporated with

20 and 40 mm air cavity gaps were modelled using an air model from COMSOL's material library. The calculated SAC spectra for specimens are depicted in Figure 16c to f. These illustrations validate a consistent shift in the SAC spectra towards lower frequencies as air cavity thickness increases, analogous to experimental spectra observations. Additionally, visualisations of the sound pressure level (SPL) at the resonance frequency are combined with the SAC spectra, indicating concentrated sound pressure at the specimen domain, which indicates effective absorption at certain frequencies. This analysis corroborates the numerical predictions based on the Attenborough model regarding the influence of material and structural changes on the specimen's absorption efficiency. Additionally, this investigation provides insights into SPL distribution during the evaluation of 3DPRC blocks, enhancing the understanding of how structural design influences acoustic performance.

For the acoustic absorption behaviours of 3DPRC with distinct built-in air cavity, the experimental and simulation results align with research findings by Mvubu M et al. [56], Sanchis E et al. [57] as well as Tang et al. [58]. The increment of the SAC can be attributed to the sound wave interference effect, while the shift of resonance frequency can then be attributed to the Helmholtz effect. The enhancement of the SAC peak value arises because when the dimensions of the air gap align with odd multiples of a quarter wavelength, a phase difference of 180° occurs between the incident and reflected waves, leading to destructive interference of sound waves and subsequent sound wave dissipation. Regarding the shift of SAC curves to lower frequency ranges, it can be explained by considering the macroscopic Helmholtz resonator formed by open pores and

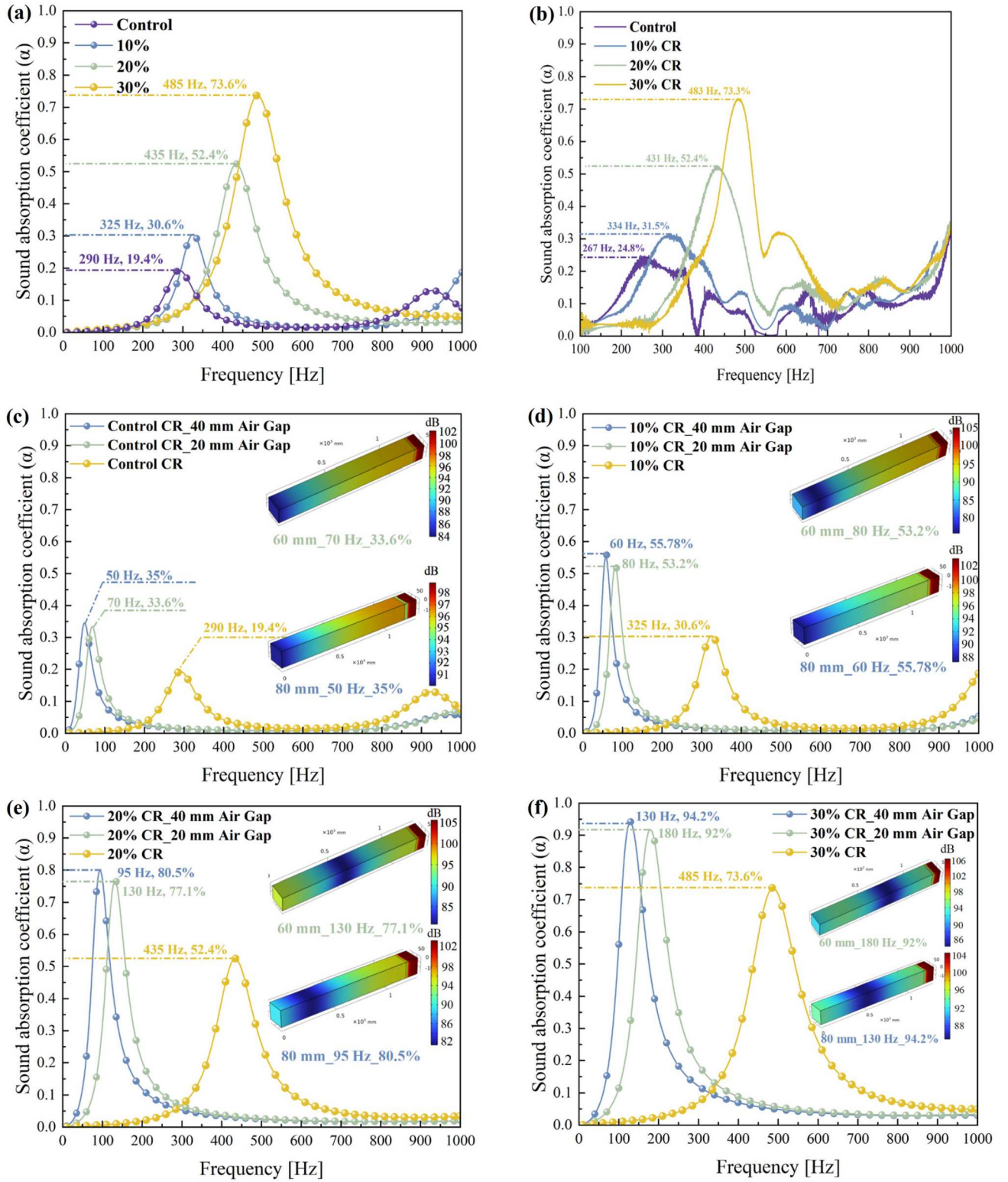


Figure 16. FEM-based acoustic absorption simulation results: (a) simulated SAC spectrums; (b) experimental SAC spectrums; SAC spectrums for (c) control group; (d) 10% CR group; (e) 20% CR group; (f) 30% CR group with a distinct air gap.

penetrating pores as channels and the air gap as the cavity. The frequency of acoustic resonance within the Helmholtz resonator can be calculated from the expression 10, where V_0 represents the volume of the

cavity, and L_0 and S_0 denote the length and width of the channel respectively. Therefore, with the increase of the volume of cavity (V_0) in the Helmholtz resonator, the resonance frequency (f) of acoustic wave within

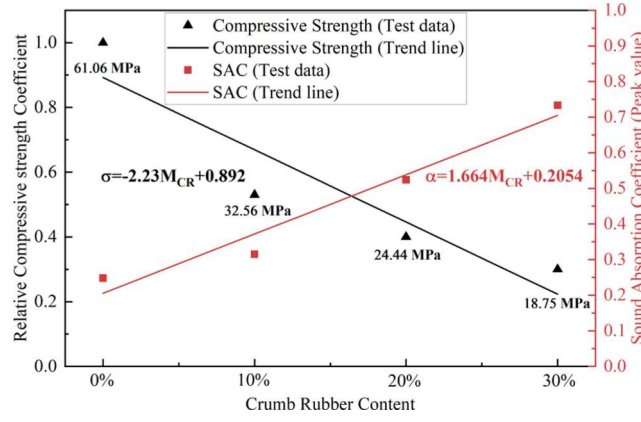


Figure 17. Correlation between compressive strength and sound absorption coefficient for 3DPRC with distinct CR content.

the structure would decrease to a lower range.

$$f = \frac{1}{2\pi} \sqrt{c^2 \frac{S_0}{V_0 L_0}} \quad (10)$$

Mirjalili et al. [59] demonstrated that increasing wall thickness enhances the SAC across all frequencies, primarily by increasing the distance over which sound energy dissipates. Apart from this, previous studies [57, 58] adopted air gaps at the back of specimens to achieve better sound absorption performance. Nevertheless, in this study it was found that the utilisation of 3D-printed sound insulation blocks with built-in air cavities achieves similar improvements in SAC, thereby conserving material resources. This approach offers a more convenient manufacturing process and holds promise for broader engineering applications, enabling the realisation of complex geometric and lattice structures. The development and validation of the effects of air-gap structures on sound absorption behaviours established a solid foundation for future research.

6.3. Optimal CR content determination analysis

Based on the data obtained from uniaxial compressive tests (UCTs) and acoustic impedance tube tests, a regression analysis was conducted to establish the relationship between crumb rubber content and both relative compressive strength coefficient and peak sound absorption coefficient. As shown in Figure 17, there is a noticeable negative trend in compressive strength as the crumb rubber content increases within the 3DPRC. Conversely, a positive trend is observed for the sound absorption coefficient (SAC) as crumb rubber content increases. It is significant to highlight that normalisation of the true compressive strength was carried out to facilitate accurate computation of

the linear model and to determine the optimal crumb rubber content. For clarity and enhanced analysis, the true compressive strength values were specifically marked in the figure.

The compressive strength model for 3DPRC with varying crumb rubber content is represented by Eq. (11), while the model for the sound absorption coefficient is captured in Eq. (12). Utilising these models, the optimal crumb rubber replacement ratio was calculated as 17.63% by determining the intersection point of the two linear equations. Given considerations for experimental accuracy and practical engineering applications, the optimal crumb rubber content for 3DPRC is recommended to be between 15% and 20%, where the corresponding range of compressive strength is 24MPa–34 MPa and range of SAC is 0.455–0.524. Within this range, the material maintains sufficient mechanical properties for use as a structural wall and exhibits considerable acoustic absorption capabilities suitable for sound-absorptive applications. Additionally, 3DPRC with 15%–20% CR content has also demonstrated effective sound insulation properties, as depicted in Figure 12a. The proposed equations relating compressive strength and sound absorption coefficient to CR content are as follows:

$$\sigma = -2.23M_{CR} + 0.892 \quad R^2 = 86.4\% \quad (11)$$

$$\alpha = 1.664M_{CR} + 0.2054 \quad R^2 = 95.8\% \quad (12)$$

where σ is the relative compressive strength coefficient, α is the sound absorption coefficient and M_{CR} is the CR replacement fraction.

It can be found that the coefficient of determination R^2 of the proposed models are 86.4% and 95.8%, respectively. For compressive model, more experimental data are required to obtain a better regression to predict the relationship more accurately between the compressive strength and CR content.

Table 6. Mixing proportion and price of the 3DPRC materials in this study.

| Material compositions | Control | 10% CR | 20% CR | 30% CR | Material price (US \$/ton) $P_{material}$ |
|-----------------------------------|---------|-------------------------------|--------|--------|--|
| | | $K_{proportion\ coefficient}$ | | | |
| Cement | 1 | 1 | 1 | 1 | 92 |
| Fly ash | 1 | 1 | 1 | 1 | 92 |
| Silica fume | 0.025 | 0.025 | 0.025 | 0.025 | 8 |
| Sand | 0.51 | 0.46 | 0.408 | 0.356 | 295 |
| Crumb rubber | 0 | 0.051 | 0.102 | 0.154 | 242 |
| Water/Cement Ratio | 0.305 | 0.305 | 0.305 | 0.305 | - |
| Total cost to produce 1 Ton 3DPRC | 132.41 | 131.40 | 130.27 | 129.19 | |

6.4. Economic assessment of the 3DPRC material

The economic efficiency is evaluated by comparing the cost of cementitious materials between different 3DPRC groups with distinct crumb rubber replacement ratios. The price of the material and proportion coefficient ($K_{proportion\ coefficient}$) of 3DPRC in this study are listed in Table 6. This economic analysis method on the 3DPRC material was also utilised in the research conducted by Liu et al. [60].

The price of the raw materials in Table 6 are obtained from the supplier which is aligned with the commercial price in the Singapore market. The cost (US\$) per ton of raw materials for 3DPRC can be calculated by using Eq. (13).

$$P_{formula} = \frac{\sum (P_{materials} \times K_{proportional-coefficient})}{\sum K_{proportional-coefficient}} \quad (13)$$

The data presented in Table 6 illustrates a decreasing trend in the total cost of producing one ton of 3DPRC as the crumb rubber replacement ratio increases. Therefore, substituting natural aggregate with waste crumb rubber not only reduces the cost of raw materials but also facilitates the conversion of this potentially hazardous waste into a functional construction material. This approach emphasises the economic and environmental benefits of integrating recycled materials into building processes.

7. Conclusion

This research elaborately designed and prepared a series of 3D-printed rubberised cementitious composites (3DPRC) with outstanding acoustic absorption and insulation performance. By conducting uniaxial compression test (UCT), SEM test, μ CT test, and impedance tube test, the compressive strength, interfacial region area, pore parameters, Sound Absorption Coefficient (SAC), and Sound Transmission Loss (STL) were determined.

Additionally, the mechanisms and efficiency of sound absorption of 3DPRC correlated to microstructural properties compared to those of cast concrete were discussed in this study. Specific findings are shown as follows.

- 1) Overall, the compressive strength decreases with the increase of crumb rubber content. The pretreatment condition shows noteworthy impact on the compressive strength of 3DPRC. NaOH pretreatment method is more effective when compared with the water treatment method. Furthermore, the toughness of the 3DPRC is proved to increase with the increase of CR content. The alterations of the interfacial gap between the pretreated rubber surface and cement matrix, observed under SEM images, further explain the mechanical properties of the 3DPRC.
- 2) The overall Noise Reduction Coefficient (NRC) display a rising trend as the CR content increases. An increasing trend of the frequency associated with the peak in SAC curves was observed. Additionally, the built-in air cavity plays a significant role in enhancing the peak value of the SAC and decreasing the resonance frequency to a lower range.
- 3) Numerical simulations demonstrate a commendable concordance between experimental and simulated SAC values, which are related to various material properties and structures. Three mechanisms of acoustic absorption in the microscopic pore structure of 3DPRC were proposed with the aid of the Helmholtz resonator principle and μ -CT results.
- 4) CR content as well as the thickness of the built-in air cavity have positive contributions to the sound insulation properties of 3DPRC. Nevertheless, it is found that the sound insulation of 3DPRC with 30% CR is insignificant, which can be attributed to the fact that high porosity dominates the impact of STL for 3DPRC.

This study examined the mechanical and acoustic properties of 3D-printed rubberised cementitious composites (3DPRC). The experimental findings suggest that 3DPRC with a range of 15%–20% crumb rubber content represents the optimal group, balancing effective sound absorption and insulation with substantial mechanical properties. While 3DPRC with 30% crumb rubber content exhibits superior sound absorption characteristics, its significantly lower compressive strength relative to the control group restricts its use in structural components. With the identified optimal material composition for 3DPRC, future research will explore the impact of topologically optimised geometries on sound insulation and absorption. The

integration of 3D concrete printing with topology optimisation holds promise for enhancing the practical applications of 3D printed rubberised concrete structures in engineering.

CRediT authorship contribution statement

Xiangyu WANG: Writing – review & editing, Writing – original draft, Conception; Investigation; Formal Analysis; Methodology; Liangfen Du: Investigation, Formal analysis, Data curation; Zhenbang Liu: Investigation, Formal analysis, Data curation; Mingyang Li: Writing – review & editing, Supervision, Methodology, Investigation; Yiwei Weng: Investigation, Formal analysis, Data curation; Zhixin Liu: Investigation, Formal analysis, Data curation; Yi Wei Daniel Tay: Investigation, Data Curation; Zheng Fan: Writing – review & editing; Ming Jen Tan: Writing – review & editing, Supervision, Funding acquisition. Teck Neng Wong: Writing – review & editing, Supervision, Funding acquisition.

Data availability

The raw/processed data of this study are available from the corresponding author upon reasonable request.

Disclosure statement

The authors declare that they have no known competing financial interests or personal relationships that could have appeared to influence the work reported in this paper.

Funding

This research is supported by the National Research Foundation, Singapore, Prime Minister's Office, Singapore, under its Medium-Sized Centre funding scheme, Singapore Centre for 3D Printing, Chip Eng Seng Corporation Ltd., CES_SDC Pte. Ltd., and CES_INNOVFAB Pte. Ltd.

ORCID

Mingyang Li  <http://orcid.org/0000-0003-1507-1509>
Yi Wei Daniel Tay  <http://orcid.org/0000-0002-7369-2138>

References

- [1] by Balamurugan Darshini Supervisor, L. Bu Sung, SCSE21-0956 Study of soundscape in singapore and its correlation to urbanization policies, with a focus on noise modelling and noise perception, 2022.
- [2] Ascari E, Licitra G, Teti L, et al. Low frequency noise impact from road traffic according to different noise prediction methods. *Sci Total Environ.* 2015;505:658–669. doi:10.1016/j.scitotenv.2014.10.052
- [3] Münzel T, Sørensen M, Daiber A. Transportation noise pollution and cardiovascular disease. *Nat Rev Cardiol.* 2021;18:619–636. doi:10.1038/s41569-021-00532-5
- [4] Wang H, Wu Z, Chen J, et al. Evaluation of road traffic noise exposure considering differential crowd characteristics. *Transp Res Part D Transp Environ.* 2022;105; doi:10.1016/j.trd.2022.103250
- [5] Wang C, Pang W, Ma Z, et al. Investigation on mechanical behaviors of a new sustainable composite material for fiber-reinforced recycled aggregate concrete under compressive low-cycle loadings. *Constr Build Mater.* 2022;326:126916, doi:10.1016/j.conbuildmat.2022.126916
- [6] Wang C, Xiao J, Liu W, et al. Unloading and reloading stress-strain relationship of recycled aggregate concrete reinforced with steel/polypropylene fibers under uniaxial low-cycle loadings. *Cem Concr Compos.* 2022;131:104597, doi:10.1016/j.cemconcomp.2022.104597
- [7] Wang C, Zhang Y, Ma Z, et al. Hysteretic deteriorating behaviors of fiber-reinforced recycled aggregate concrete composites subjected to cyclic compressive loadings. *J Build Eng.* 2022;49:104087, doi:10.1016/j.jobbe.2022.104087
- [8] Wang C, Du Z, Zhang Y, et al. Elaborating the 3D microstructural characteristics and strength softening mechanical mechanism of fiber-reinforced recycled aggregate concrete. *Constr Build Mater.* 2024;436:137009, doi:10.1016/j.conbuildmat.2024.137009
- [9] Wang J, Du B. Experimental studies of thermal and acoustic properties of recycled aggregate crumb rubber concrete. *J Build Eng.* 2020;32; doi:10.1016/j.jobbe.2020.101836
- [10] Ling TC, Nor HM, Lim SK. Using recycled waste tyres in concrete paving blocks. *Proc Inst Civ Eng: Waste Resour Manag.* 2010;163:37–45. doi:10.1680/warm.2010.163.1.37
- [11] Sukontasukkul P. Use of crumb rubber to improve thermal and sound properties of pre-cast concrete panel. *Constr Build Mater.* 2009;23:1084–1092. doi:10.1016/j.conbuildmat.2008.05.021
- [12] Assaggaf RA, Ali MR, Al-Dulaijan SU, et al. Properties of concrete with untreated and treated crumb rubber – A review. *J Mat Res Technol.* 2021;11:1753–1798. doi:10.1016/j.jmrt.2021.02.019
- [13] Wang L, Lu B, Wang X, et al. Evaluation of 3D robotic spray parameters on the performance of the developed sensing functional cementitious coating. *Virtual Phys Prototyp.* 2024;19:e2383969, doi:10.1080/17452759.2024.2383969
- [14] Liu Z, Li M, Wang X, et al. Axial performances of the steel rebar reinforced column confined by the steel cable reinforced 3D concrete printing permanent formwork. *Virtual Phys Prototyp.* 2024;19:e2382163, doi:10.1080/17452759.2024.2382163
- [15] Lu B, Wang L, Wang X, et al. Development of robotic sprayable self-sensing cementitious material for smart structural health monitoring. *Additive Manufacturing.* 2024;85:104161, doi:10.1016/j.addma.2024.104161
- [16] Tay YWD, Panda B, Paul SC, et al. 3D printing trends in building and construction industry: a review. *Virtual Phys Prototyp.* 2017;12:261–276. doi:10.1080/17452759.2017.1326724

- [17] Geng Z, Wu P, Pan H, et al. Robust layer interface in cement additive manufacturing via silicate penetration and precipitation. *Mater Des.* 2022;214; doi:10.1016/j.matdes.2022.110380
- [18] Liu Z, Li M, Quah TKN, et al. Comprehensive investigations on the relationship between the 3D concrete printing failure criterion and properties of fresh-state cementitious materials. *Additive Manufacturing.* 2023;76:103787, doi:10.1016/j.addma.2023.103787
- [19] Geng Z, She W, Zuo W, et al. Layer-interface properties in 3D printed concrete: dual hierarchical structure and micromechanical characterization. *Cem Concr Res.* 2020;138; doi:10.1016/j.cemconres.2020.106220
- [20] Geng Z, Pan H, Zuo W, et al. Functionally graded lightweight cement-based composites with outstanding mechanical performances via additive manufacturing. *Additive Manufacturing.* 2022;56; doi:10.1016/j.addma.2022.102911
- [21] Weng Y, Li M, Liu Z, et al. Printability and fire performance of a developed 3D printable fibre reinforced cementitious composites under elevated temperatures. *Virtual Phys Prototyp.* 2019;14:284–292. doi:10.1080/17452759.2018.1555046
- [22] Kruger J, du Plessis A, van Zijl G. An investigation into the porosity of extrusion-based 3D printed concrete. *Additive Manufacturing.* 2021;37; doi:10.1016/j.addma.2020.101740
- [23] Liu Z, Li M, Wong TN, et al. Determine the effects of pore properties on the mechanical performances of 3D concrete printing units with experimental and numerical methods. *J Build Eng.* 2024;92:109730, doi:10.1016/j.jobe.2024.109730
- [24] Liu C, Zhang R, Liu H, et al. Analysis of the mechanical performance and damage mechanism for 3D printed concrete based on pore structure. *Constr Build Mater.* 2022;314:125572, doi:10.1016/j.conbuildmat.2021.125572
- [25] ASTM E2611–17. Standard Test Method for Normal Incidence Determination of Porous Material Acoustical Properties Based on the Transfer Matrix Method, ASTM International PA, 2017.
- [26] S. Standard. EN ISO 10534-2, Determination of sound absorption coefficient and acoustic impedance with the interferometer, 2001.
- [27] GBT 14684, (2022).
- [28] Wang C, Wu H, Li C. Hysteresis and damping properties of steel and polypropylene fiber reinforced recycled aggregate concrete under uniaxial low-cycle loadings. *Constr Build Mater.* 2022;319:126191, doi:10.1016/j.conbuildmat.2021.126191
- [29] Liu J, Setunge S, Tran P. 3D concrete printing with cement-coated recycled crumb rubber: compressive and microstructural properties. *Constr Build Mater.* 2022;347; doi:10.1016/j.conbuildmat.2022.128507
- [30] Youssf O, Mills JE, Hassanli R. Assessment of the mechanical performance of crumb rubber concrete. *Constr Build Mater.* 2016;125:175–183. doi:10.1016/j.conbuildmat.2016.08.040
- [31] Wolfs RJM, Bos FP, Salet TAM. Hardened properties of 3D printed concrete: The influence of process parameters on interlayer adhesion. *Cem Concr Res.* 2019;119:132–140. doi:10.1016/j.cemconres.2019.02.017
- [32] Aslani F, Dale R, Hamidi F, et al. Mechanical and shrinkage performance of 3D-printed rubberised engineered cementitious composites. *Constr Build Mater.* 2022;339:127665, doi:10.1016/j.conbuildmat.2022.127665
- [33] Jiang Q, Liu Q, Wu S, et al. Modification effect of nanosilica and polypropylene fiber for extrusion-based 3D printing concrete: printability and mechanical anisotropy. *Additive Manufacturing.* 2022;56:102944, doi:10.1016/j.addma.2022.102944
- [34] Liu Q, Jiang Q, Huang M, et al. Modifying effect of anionic polyacrylamide dose for cement-based 3DP materials: printability and mechanical performance tests. *Constr Build Mater.* 2022;330:127156, doi:10.1016/j.conbuildmat.2022.127156
- [35] Crivoi A, Du L, Fan Z. Ventilated acoustic meta-barrier based on layered helmholtz resonators. *Appl Acoust.* 2023;205; doi:10.1016/j.apacoust.2023.109263
- [36] Gourlay E, Glé P, Marceau S, et al. Effect of water content on the acoustical and thermal properties of hemp concretes. *Constr Build Mater.* 2017;139:513–523. doi:10.1016/j.conbuildmat.2016.11.018
- [37] Najim KB, Hall MR. Crumb rubber aggregate coatings/pre-treatments and their effects on interfacial bonding, air entrapment and fracture toughness in self-compacting rubberised concrete (SCRC). *Mater Struct.* 2013;46:2029–2043. doi:10.1617/s11527-013-0034-4
- [38] Chen YX, Wu F, Yu Q, et al. Bio-based ultra-lightweight concrete applying miscanthus fibers: acoustic absorption and thermal insulation. *Cem Concr Compos.* 2020;114:103829, doi:10.1016/j.cemconcomp.2020.103829
- [39] Zhao J, Wang XM, Chang JM, et al. Sound insulation property of wood-waste tire rubber composite. *Compos Sci Technol.* 2010;70:2033–2038. doi:10.1016/j.compscitech.2010.03.015
- [40] Mohammed BS, Anwar Hossain KM, Eng Swee JT, et al. Properties of crumb rubber hollow concrete block. *J Clean Prod.* 2012;23:57–67. doi:10.1016/j.jclepro.2011.10.035
- [41] Koruk H, Ozcan AC, Genc G, et al. Jute and luffa fiber-reinforced biocomposites: effects of sample thickness and fiber/resin ratio on sound absorption and transmission loss performance. *J Nat Fibres.* 2022;19:6239–6254. doi:10.1080/15440478.2021.1907832
- [42] Zhou J, Bhaskar A, Zhang X. Optimization for sound transmission through a double-wall panel. *Appl Acoust.* 2013;74:1422–1428. doi:10.1016/j.apacoust.2013.06.002
- [43] Wang Z, Xie J, Gao L, et al. Study on sound absorption model of porous asphalt concrete based on three-dimensional morphology of air voids. *Constr Build Mater.* 2022;338; doi:10.1016/j.conbuildmat.2022.127537
- [44] Arenas, J.P. and Crocker, M.J., Recent trends in porous sound-absorbing materials, *Sound & Vibration* 44 (2010) 12–18.
- [45] Sambucci M, Valente M. Acoustic behaviour of 3d-printable cement mortars functionalized with recycled tire rubber aggregates, n.d.
- [46] Asdrubali F, Baldinelli G, D'Alessandro F. Evaluation of the acoustic properties of materials made from recycled tyre granules, *Internoise Ince*, 2007.
- [47] Mukhametrakhimov RK, Lukmanova LV. Structure and properties of mortar printed on a 3D printer. *Mag Civ Eng.* 2021;102; doi:10.34910/MCE.102.6

- [48] Amran M, Fediuk R, Murali G, et al. Sound-Absorbing acoustic concretes: A review. *Sustainability*. 2021;13:10712, doi:[10.3390/su131910712](https://doi.org/10.3390/su131910712)
- [49] Fediuk R, Amran M, Vatin N, et al. Acoustic properties of innovative concretes: A review. *Materials*. 2021;14:398, doi:[10.3390/ma14020398](https://doi.org/10.3390/ma14020398)
- [50] Chen JH, Liu PS, Sun JX. Sound absorption performance of a lightweight ceramic foam. *Ceram Int*. 2020;46:22699–22708. doi:[10.1016/j.ceramint.2020.06.033](https://doi.org/10.1016/j.ceramint.2020.06.033)
- [51] Elkhateeb A, Adas A, Attia M, et al. Absorption characteristics of masjid carpets. *Appl Acoust*. 2016;105:143–155. doi:[10.1016/j.apacoust.2015.12.005](https://doi.org/10.1016/j.apacoust.2015.12.005)
- [52] Berardi U, Iannace G. Acoustic characterization of natural fibers for sound absorption applications. *Build Environ*. 2015;94:840–852. doi:[10.1016/j.buildenv.2015.05.029](https://doi.org/10.1016/j.buildenv.2015.05.029)
- [53] Barrigón Morillas JM, Montes González D, Vilchez-Gómez R, et al. Virgin natural cork characterization as a sustainable material for Use in acoustic solutions. *Sustainability*. 2021;13:4976, doi:[10.3390/su13094976](https://doi.org/10.3390/su13094976)
- [54] Huang Y, Zhou D, Xie Y, et al. † † Moe, Tunable Sound Absorption of Silicone Rubber Materials via Mesoporous Silica, n.d.
- [55] Voronina NN, Horoshenkov KV. A new empirical model for the acoustic properties of loose granular media, n.d. www.elsevier.com/locate/apacoust.
- [56] Mvubu MB, Anandjiwala R, Patnaik A. Effects of air gap, fibre type and blend ratio on sound absorption performance of needle-punched non-woven fabrics. *J Eng Fiber Fabr*. 2019;14; doi:[10.1177/1558925019840874](https://doi.org/10.1177/1558925019840874)
- [57] Sanchis EJ, Alcaraz JS, Belda IM, et al. Sustainable multiple resonator sound absorbers made from fruit stones and air gap. *Alexandria Eng J*. 2022;61:10219–10231. doi:[10.1016/j.aej.2022.03.063](https://doi.org/10.1016/j.aej.2022.03.063)
- [58] Tang X, Zhang X, Zhang H, et al. Corn husk for noise reduction: robust acoustic absorption and reduced thickness. *Appl Acoust*. 2018;134:60–68. doi:[10.1016/j.apacoust.2018.01.012](https://doi.org/10.1016/j.apacoust.2018.01.012)
- [59] Abbas Mirjalili S, Mohammad-Shahi M. Investigation on the Acoustic Characteristics of Multi-Layer Nonwoven Structures. Part 1-Multi-Layer Nonwoven Structures with the Simple Configuration, n.d.
- [60] Liu Q, Jiang Q, Huang M, et al. The fresh and hardened properties of 3D printing cement-base materials with self-cleaning nano-TiO₂:An exploratory study. *J Clean Prod*. 2022;379:134804, doi:[10.1016/j.jclepro.2022.134804](https://doi.org/10.1016/j.jclepro.2022.134804)